Department of Precision and Microsystems Engineering

Automated Reset Controller Design in the Frequency Domain

Bas Cheizoo

Report no : 2024.027
Coaches : ir. Luke van Eijk and ir. Kai Wa Yan
Professor : dr. ir. Hassan HosseinNia Kani
Specialisation : Mechatronic System Design
Type of report : MSc. Thesis
Date : May 27th, 2024

Automated Reset Controller Design in the Frequency Domain

MSc. Thesis

Bas Cheizoo

May 27th, 2024

Faculty of Mechanical Engineering · Delft University of Technology

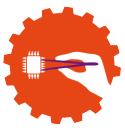

Acknowledgements

First and foremost, I would like to express my profound gratitude to my daily supervisor, Luke van Eijk, for creating a remarkable environment in which I was entrusted with the opportunity to grow independently while receiving the critical, constructive, and exceptionally thorough feedback needed to steer me in the right direction at all stages of the project and at the level I desired. His admirable supervision, which combined trust and autonomy, provided the space I needed to develop my skills, yet I could always seek and receive guidance when necessary.

Secondly, I would like to thank the range of other supervisors that have played an important role in the progress of my thesis; Kai Wa Yan, Hassan HosseinNia Kani, and Dragan Kostić. With biweekly and monthly meetings that brought new insights and ideas to mind, I was provided ample guidance to bring me to the final result I present to you, the reader, through this thesis.

Lastly, I would like to thank the company ASMPT for providing the use cases to validate my research. The modelled Simscape Multibody and physical wire bonders provided valuable insight into the effectiveness of my work and provided the means to see the theory in action.

Delft, University of Technology — Bas Cheizoo
May 27th, 2024

Abstract

The speed and precision required in the precision motion industry is an ever-growing challenge. Linear control offers intuitive frequency-domain controller design methods that are based on a frequency response function (FRF) of the plant, which is obtained solely from measurement data. Unsurprisingly, linear controllers account for over 90 % of the controllers currently used in the industry. However, as linear controllers are subject to inherent performance limitations such as Bode's gain-phase relationship and the waterbed effect, research on nonlinear control solutions to overcome these limitations is ubiquitous. Reset control first showed up in 1958 with the Clegg integrator (CI). According to a sinusoidal-input-describing-function analysis, the CI provides reduced phase lag compared to a linear integrator, suggesting Bode's gain-phase relationship can be overcome and consequently allowing for performance surpassing that of linear control systems. The drawbacks of the CI are the possible emergence of limit cycles and the excitation of high-frequent modes of the system originating from higher-order harmonics of the CI's input caused by discontinuities in the control signal. The generalised-first-order-reset-element-based integrator (GFbI) is the only reset element that can prevent the emergence of limit cycles and can reduce the generation of higher-order harmonics, whilst retaining the advantageous reduced phase lag the CI provides and allowing for closed-loop controller design based on a plant FRF while taking the effects of higher-order harmonics into account, matching the design methods of linear controllers. Optimally tuning a reset controller is a complex and time-consuming task. Moreover, established tuning rules are still lacking. This work facilitates designing a reset controller containing a GFbI element by providing two contributions to utilise the potential of the GFbI element to improve upon linear control. The first is a comparative study on the effect of the controller element sequence, aimed at reducing the negative consequences of the higher-order harmonics generated by the reset element. The second is the proposal of an FRF-based optimisation algorithm utilising frequency-domain performance prediction methods to automatically tune a reset controller containing a GFbI element to adhere to the imposed constraints and maximise the benefit gained from the nonlinear element. Validation using a simulated and physical wire bonder showed the algorithm successfully tuned four different reset controllers using two different sequences. The performance of the tuned reset controllers was compared to that of equally-well-tuned linear controllers. In the first use case with the goal of suppressing a dominant vibration in the error signal, the median root-mean-square error was reduced by 16.245 %. In the second use case, the goal was to improve the settling time, which was achieved by a median of 9.791 %. The best results were achieved using a sequence in which the higher-order harmonics were avoided from passing through the lead filter in open loop, mitigating amplification thereof. The proposed tuning algorithm proved able to tune reset controllers containing a GFbI element such that the performance of linear control based on frequency-domain performance prediction metrics was surpassed, where two use cases confirmed the predicted performance increase through time-domain simulations and experiments on a physical setup.

Table of Contents

Chapter 1

Introduction

Linear time-invariant (LTI) controllers dominate the current precision motion control industry [1]. Applications include automotive, aviation, process control, semiconductor equipment manufacturing, etc. Specifically, proportional-integral-derivative (PID) controllers account for over 90 % of controllers currently used in the industry. This is rightfully so, as among others, such controllers lend themselves for loop-shaping-based design in a closed-loop system based solely on a frequency response function (FRF) of the plant. Loop-shaping is an intuitive controller design method using performance prediction in the frequency domain based on the sensitivity function.

LTI controllers are inherently limited due to their linear nature. Two of these limitations are the waterbed effect and Bode's gain-phase relationship [2, 3]. As the development of LTI control steadily progresses, it becomes increasingly challenging to continue improving LTI control due to its inherent limitations and diminishing returns are prevalent. Nonlinear time-invariant (NLTI) solutions may be key to improving further upon LTI control.

Reset control is an NLTI control technique that has shown the potential to overcome LTI limitations [4]. First introduced by Clegg in 1958 [5], the simplest form of reset control is a Clegg integrator (CI). The CI follows the behaviour of a linear integrator, with the addition of resetting its state whenever its input hits zero. The behaviour of a nonlinear element can be analysed using a sinusoidal-input describing function (SIDF) analysis [6]. An SIDF analysis of the CI shows the element exhibits a phase lag of 38.1 degrees while providing the same magnitude response as a linear integrator, which is a significant improvement upon the familiar 90 degree phase lag of a linear integrator.

The reduced phase lag of the CI comes at a cost. Firstly, as every state reset is essentially a step in the control signal, more frequencies are excited than contained in the input sinusoid [7]. As a result, the output of the CI contains higher-order harmonics of its input that are injected into the plant. These higher-order harmonics are neglected by an SIDF analysis. Using a higher-order SIDF (HOSIDF) description of the CI's output [7], these higher-order harmonics can be captured. The HOSIDF description allows for accurate closed-loop loop-shaping through the use of the pseudo-sensitivity [8], providing a means to analyse and subsequently mitigate the drawback of the higher-order harmonics. Secondly, state resets can cause the emergence of limit cycles in a closed loop reset control system (RCS) [9].

The focus of this work is on NLTI control techniques for which closed-loop controller design based on solely a plant FRF is possible and for which a HOSIDF analysis is possible. Two reset-

based control structures exist that fall under this class of nonlinear elements and that have shown to mitigate both drawbacks of the CI. The first is a combination of a linear proportional-integral (PI) and nonlinear CI element to form a PI+CI element [10]. This element divides the integral action over the two integrators, posing a direct trade-off between reducing the higher-order harmonics and reducing the phase lag. The second is a combination of a PI element and a generalised first-order reset element (GFORE) to form a GFORE-based integrator (GFbI) element [11]. This element provides integral action from the PI element up to a tuneable phase-shift frequency, after which the GFORE dominates and provides integral action for the rest of the frequency spectrum. This structure trades off rather than shares the integral action between the linear and nonlinear elements. Whilst providing the same magnitude response as a PI element, SIDF analysis shows the GFbI element exhibits a phase lag of 90 degrees prior to and 38.1 degrees after the phase-shift frequency. As the reduced phase lag is only needed around the bandwidth frequency, the drawbacks of the state resets can be mitigated without trading off the advantage. This behaviour makes the GFbI element preferable over the direct trade-off posed by a PI+CI element. The only remaining alternative is a similar control structure to the GFbI that uses hybrid integrator-gain systems (HIGS) instead of a GFORE [12, 13]. However, based on an SIDF analysis, the phase lag of a GFORE can be tuned between -90 and 0 degrees, while for HIGS the phase lag is limited to between -90 and -38.15 degrees. Additionally, in contrast to the GFbI element, the effects of the higher-order harmonics generated by the HIGS cannot clearly be analysed for a closed-loop system. This also makes the GFbI preferred over a solution using HIGS.

Established tuning rules for reset controllers are still lacking. Even if they existed, such rules generally lead to sub-optimal designs. Optimally tuning a linear controller by hand can be a cumbersome and time-consuming task, let alone doing so for a reset controller. This work facilitates designing a reset controller containing a GFbI element. Two contributions are provided that investigate the potential benefits of using a GFbI element to improve upon LTI control. Firstly, a comparative study is provided on the effect of different controller element sequences on the generation of higher-order harmonics. A key insight to this is the amplification of higher-order harmonics by a lead filter, which can be mitigated by placing the lead filter in parallel to the reset element. Secondly, an algorithm is proposed to gain maximum advantage from the benefits of a GFbI element in an automated and intuitive fashion.

The remainder of this work is structured as follows. Chapter 2 provides the necessary preliminaries on linear and reset control. Subsequently, the comparative study of different controller element sequences is given in Chapter 3. The tuning algorithm is proposed in Chapter 4. The contributions are validated using both a simulated and physical plant in Chapter 5. Finally, concluding remarks are provided in Chapter 6, along with future research recommendations.

Chapter 2

Preliminaries

This chapter focuses on the preliminaries of linear and reset control. The required details on linear control is provided in Section 2-1. Subsequently, the necessary background on reset control is given in Section 2-2.

2-1 Linear control

This section elaborates on the preliminaries of linear control. The basics are detailed in Section 2-1-1, followed by a brief overview of inherent limitations of linear control in Section 2-1-2.

2-1-1 Basics of linear control

A linear feedback control system has numerous traits that make it attractive for industrial applications. For example, linear systems allow using the principle of superposition [14, Chapter 5]. Additionally, closed-loop performance prediction using the sensitivity function, further simply called the sensitivity, is possible based on solely the FRF of the plant. The sensitivity offers an intuitive controller design method, namely loop-shaping. For example, an observed vibration in the error signal can be suppressed simply by reducing the sensitivity at that frequency. Moreover, analysing closed-loop stability can also be done using the plant FRF.

Figure 2-1 shows the control architecture of a basic feedback and feedforward control loop. In the figure, $r \in \mathbb{R}$ denotes the reference signal, $u \in \mathbb{R}$ the undisturbed control signal, $d \in \mathbb{R}$ a disturbance signal, $y \in \mathbb{R}$ the real output signal, $n \in \mathbb{R}$ a noise signal, $y^* \in \mathbb{R}$ the noise-corrupted output signal and $e = r - y^* \in \mathbb{R}$ the error signal. The error signal goes into the single-input single-output (SISO) LTI *feedback* controller C_{fb}. Furthermore, C_{ff} denotes the SISO LTI *feedforward* controller. Lastly, G denotes the SISO LTI plant.

As evident from Figure 2-1, the noisy output and reference signals are fed to the feedback controller to compute the control signal. The open-loop transfer function is defined as $L(s) = C_{\text{fb}}(s)G(s)$, where $s \in \mathbb{C}$ represents the Laplace variable. The sensitivity $S(s)$ is defined as

$$S(s) = \frac{\mathcal{L}\{e\}}{\mathcal{L}\{r\}} = -\frac{\mathcal{L}\{e\}}{\mathcal{L}\{n\}} = \frac{1}{1 + L(s)}, \qquad (2\text{-}1)$$

with $\mathcal{L}\{x\}$ denoting the Laplace transform of signal x.

Generally, the goal of any feedback system is to track a (known) reference signal as well as possible. The sensitivity is an insightful tool to assess the reference tracking and noise amplification of an LTI controller. For mechanical systems, the disturbance and noise signals usually have the most power in the low- and high-frequency region, respectively [15, Chapter 4]. Good disturbance

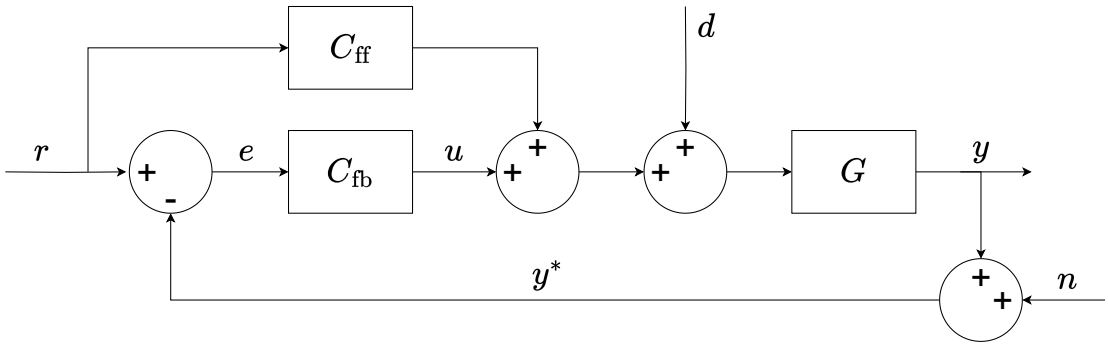

Figure 2-1: Basic feedback and feedforward control loop architecture.

rejection requires $|L(j\omega)| \gg 0$ dB in the low-frequency region, where $j = \sqrt{-1}$ and $\omega \in \mathbb{R}_{>0}$ represents a frequency. This results in $|S(j\omega)| \ll 0$ dB [14, Chapter 11, 15, Chapter 4]. Since all real systems are strictly proper, it is unavoidable to have $|L(j\omega)| \to -\infty$ dB as $\omega \to \infty$ [16, Chapter 3]. This thus results in $|S(j\omega)| \approx 0$ dB in the high-frequency region. However, the larger $|S(j\omega)|$ is, the more noise becomes visible from the error signal [14, Chapter 11]. This is especially true in the region where the noise has the most power, i.e. the high-frequency region. Therefore, it is desired to limit $|S(j\omega)|$ in that region as much as possible.

It becomes clear that there is a compromise to be made between the reference tracking capability and noise amplification of an LTI controller. For low frequencies, $|L(j\omega)| \gg 0$ dB is required for reference tracking, whereas for high frequencies, $|L(j\omega)| \ll 0$ dB is desired for noise rejection. The frequency around which the controller changes from tracking to rejecting is the bandwidth frequency ω_{bw}, such that $|L(j\omega_{\text{bw}})| = 0$ dB for the first time. The frequency region around the bandwidth is defined as the middle-frequency region. The bandwidth can thus be used as a metric for the performance of a system, provided the system is stable. Higher bandwidth generally results in improved reference tracking as the controller is active, i.e. tracking the reference, at a larger frequency range. However, this also increases the amount of measurement noise injected into the system [14, Chapter 11].

The closed-loop performance of the system can directly be seen in the sensitivity. Figure 2-2 shows the shape of a typical sensitivity function. The closed-loop performance is quantified from the sensitivity by assessing $|S(j\omega)| \ll 0$ dB. The lower the sensitivity is in the low- to middle-frequency region, the better the closed-loop performance.

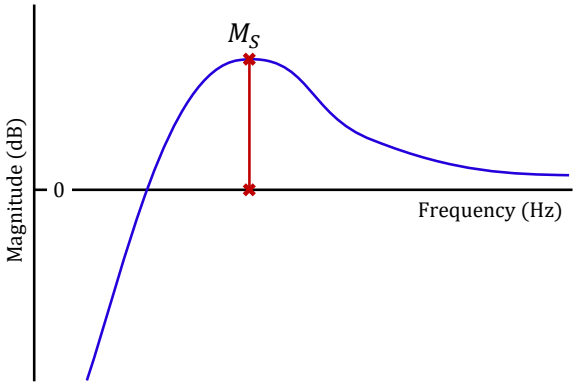

Figure 2-2: Typical sensitivity plot.

Additionally, the sensitivity provides a measure of the robustness of the system. The maximum sensitivity

$$M_S = \max_{\omega} |S(j\omega)| \tag{2-2}$$

is the peak value of the sensitivity. Equation (2-1) shows that the sensitivity is a measure for the amplification from the reference to the error signal and from the noise to the error signal. Moreover, the sensitivity and the point -1 on a Nyquist plot

of the control system are related as

$$\frac{1}{|S(j\omega)|} = d_{-1}, \tag{2-3}$$

where d_{-1} is the distance between the sensitivity at frequency ω and the point -1 on the Nyquist plot of the control system. Encircling the point -1 on the Nyquist plot of the control system indicates the control system is unstable. Thus, M_S being the *maximum* amplification of the mappings in (2-1) and the closest point to -1 on the Nyquist plot of the control system makes it suitable as a robustness metric. This relation is shown in Figure 2-3. Additionally, in all regions where the sensitivity is above 0 dB, the noise is amplified. In general, it should thus be attempted to minimise the area of the sensitivity above 0 dB to achieve good reduction of noise amplification and minimise M_S to obtain maximum robustness.

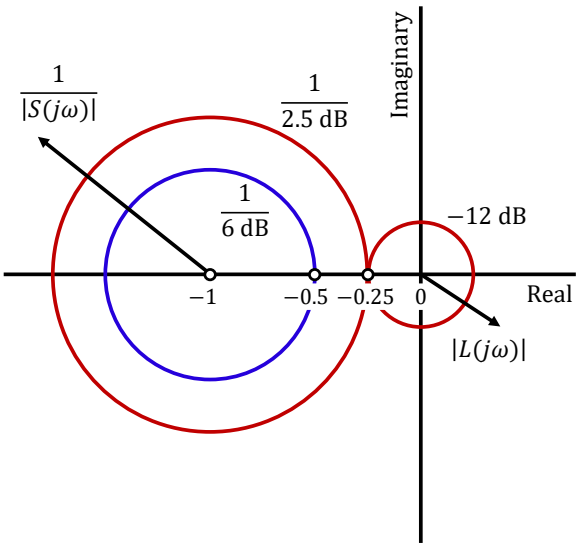

Figure 2-3: Sensitivity and open-loop constraints visualised on the complex plane. The circles around -1 represent a constant sensitivity and hence function as a constraint, as given in (2-4). The circle around the origin represents a constant open-loop gain and exactly intersects with the outer circle of constant sensitivity.

In practice, often a constraint is imposed on the maximum error amplification and minimum robustness together by limiting the maximum sensitivity. Such a constraint can be formulated as

$$M_S \leq S_{\text{lim}}, \tag{2-4}$$

where S_{lim} is the maximum allowed peak in the sensitivity. Sources like [15, Chapter 4] describe an often used S_{lim} of 6 dB, although a suitable limit may vary for each use case. The example limit of 6 dB on S_{lim} is visualised in Figure 2-3 as the blue circle. As shown, this limit corresponds to roughly $\min d_{-1} = 0.5$.

Resonances and anti-resonance of the plant often inherently come with inaccuracies in the identified plant FRF. If for a control system the maximum sensitivity is constrained, generally a more tight constraint is needed for all frequencies after the first resonance or anti-resonance of the plant to account for the inaccuracies. The frequency prior to the first resonance or anti-resonance of the plant is denoted by $\omega_{\text{res}} \in \mathbb{R}_{\geq 0}$. The exact value for ω_{res} is determined by the control system designer. The more tight sensitivity constraint for any $\omega \geq \omega_{\text{res}}$ is denoted as

$$M_{S_{\omega_{\text{res}}}} \leq S_{\text{lim}|\omega \geq \omega_{\text{res}}}, \tag{2-5}$$

where $M_{S_{\omega_{\text{res}}}}$ is the maximum sensitivity for any $\omega \geq \omega_{\text{res}}$ and is denoted as

$$M_{S_{\omega_{\text{res}}}} = \max_{\omega \in [\omega_{\text{res}}, \infty)} |S(j\omega)|. \tag{2-6}$$

An example limit of 2.5 dB on $S_{\text{lim}|\omega \geq \omega_{\text{res}}}$ is visualised in Figure 2-3 as the left red circle. As shown, this limit corresponds to roughly $\min d_{-1} = 0.5$.

Provided a control system is designed to hit the edge of $S_{\text{lim}|\omega \geq \omega_{\text{res}}}$, the plant FRF phase inaccuracy due to resonances and anti-resonances may still lead to $S_{\text{lim}|\omega \geq \omega_{\text{res}}}$ exceeding $S_{\text{lim}|\omega \geq \omega_{\text{res}}}$. To ensure the control system is robust to plant FRF phase inaccuracies, the open-loop gain can be constrained to ensure that

$$M_{L_{\omega_{\text{res}}}} \leq L_{\text{lim}|\omega \geq \omega_{\text{res}}}, \tag{2-7}$$

where $M_{L_{\omega_{\text{res}}}}$ is the maximum open-loop gain for any $\omega \geq \omega_{\text{res}}$ and is denoted as

$$M_{L_{\omega_{\text{res}}}} = \max_{\omega \in [\omega_{\text{res}}, \infty)} |L(j\omega)|. \tag{2-8}$$

The relation between $M_{S_{\omega_{\text{res}}}}$ and $M_{L_{\omega_{\text{res}}}}$ is visualised in Figure 2-3. For any $S_{\lim|\omega\geq\omega_{\text{res}}}$, a circle can be drawn around the origin, which represents $M_{L_{\omega_{\text{res}}}}$, such that the circle representing $S_{\lim|\omega\geq\omega_{\text{res}}}$ exactly intersects with the circle representing $M_{L_{\omega_{\text{res}}}}$. The resulting radius of the circle representing $M_{L_{\omega_{\text{res}}}}$ then equals the required value of $L_{\lim|\omega\geq\omega_{\text{res}}}$ to ensure that regardless of the phase of the plant, (2-7) always holds. In the case of $S_{\lim|\omega\geq\omega_{\text{res}}} = 2.5$ dB, the resulting $L_{\lim|\omega\geq\omega_{\text{res}}} = -12$ dB, as is apparent from the figure.

The control sensitivity is a measure for how much of the noise entering a control system is visible in the controller output and is defined as

$$CS(s) = -\frac{\mathcal{L}\{u\}}{\mathcal{L}\{n\}} = C_{\text{fb}}(s) \cdot S(s). \tag{2-9}$$

Essentially, the control sensitivity is a measure for how much the controller responds to noise. As shown in Figure 2-2, the sensitivity is close to 0 dB for high frequencies, thus

$$|S(j\omega_{\text{high}})| \approx 0 \text{ dB}, \tag{2-10}$$

where $S(j\omega_{\text{high}})$ is the sensitivity for a sufficiently high frequency ω_{high}. What sufficiently high exactly is depends on the control system. Consequently, the control sensitivity for any $\omega \geq \omega_{\text{high}}$ can be approximated by

$$|CS(j\omega_{\text{high}})| \approx |C(j\omega_{\text{high}})|. \tag{2-11}$$

By multiplying the control sensitivity with the plant, the relation between the control sensitivity and the open loop becomes apparent as

$$|G(j\omega_{\text{high}})| \cdot |CS(j\omega_{\text{high}})| \approx |L(j\omega_{\text{high}})|. \tag{2-12}$$

Since the plant is considered constant, the only changing variable (2-12) is the controller. In open loop, too, the only changing variable is the controller, as the plant is considered constant. Therefore, a constraint on the control sensitivity for sufficiently high frequencies can be approximated by imposing a constraint on the open loop, for the same sufficiently high frequencies. Such a constraint is denoted as

$$M_{L_{\omega_{\text{high}}}} \leq L_{\lim|\omega\geq\omega_{\text{high}}}, \tag{2-13}$$

where $M_{L_{\omega_{\text{high}}}}$ is the maximum open-loop gain for any $\omega \geq \omega_{\text{high}}$ and is denoted as

$$M_{L_{\omega_{\text{high}}}} = \max_{\omega\in[\omega_{\text{high}},\infty)} |L(j\omega)|. \tag{2-14}$$

2-1-2 Limitations of linear control

Linear control systems are subject to several constraints that are a consequence of the linear nature of such systems [2, 3]. Two are the waterbed effect and Bode's gain-phase relationship. This section further explains the origin of these two constraints and clarifies the impact they have on linear control system performance.

Waterbed effect

The sensitivity of a linear system is inherently constrained by Bode's sensitivity integral [14, Chapter 11]. The integral relation is defined as

$$\int_0^\infty \ln|S(j\omega)| \, \mathrm{d}\omega = 0. \tag{2-15}$$

Note that (2-15) is only valid for control systems that have no unstable poles and for which the open loop contains two more poles than zeros.

Equation (2-15) entails that the area of the sensitivity below 0 dB and above 0 dB must be equal on a linear diagram. This results in that either an improvement in reference tracking or reduction of noise amplification necessarily leads to a degradation of the other, as illustrated in Figure 2-4. This phenomenon is called the waterbed effect due to its analogy to how water in a waterbed can move around, but the total amount of water remains the same.

Bode's gain-phase relationship

If a linear system is stable and has minimum phase, there is a unique relationship between the phase and the gain of the system called Bode's gain-phase relationship [16, Chapter 2]. The relationship is defined as

$$\angle L(j\omega_0) = \frac{1}{\pi}\int_{-\infty}^{\infty} \frac{\mathrm{d}\ln|L(j\omega)|}{\mathrm{d}\ln\omega} \ln\left|\frac{\omega+\omega_0}{\omega-\omega_0}\right| \cdot \frac{\mathrm{d}\omega}{\omega}, \tag{2-16a}$$

$$\angle L(j\omega_0) \approx 90° \cdot N(\omega_0), \tag{2-16b}$$

where ω_0 denotes the frequency that is analysed and $N(\omega)$ is the slope in 20 dB per logarithmic decade of the magnitude on a logarithmic diagram. Equation (2-16b) gives an approximation of (2-16a). This approximation only holds if the slope near $\omega = \omega_0$ is constant, thus if there are no nearby poles or zeros.

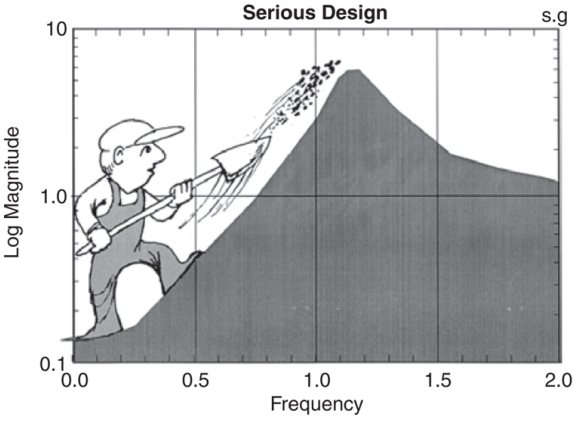

Figure 2-4: Graphical interpretation of the waterbed effect [17].

2-2 Reset control

This section focuses on the preliminaries of reset control. The general architecture of an RCS is detailed in Section 2-2-1. Subsequently, the performance prediction of an RCS is discussed in Section 2-2-2, followed by a discussion on the stability of an RCS in Section 2-2-3. Finally, Section 2-2-4 provides details on the GFbI, a novel reset element [11].

2-2-1 Reset control architecture

Beker [4] proposed a mathematical definition of a reset controller, denoted by $\mathcal{R}$, as

$$\mathcal{R} = \begin{cases} \dot{x}_{\mathrm{R}}(t) = A_{\mathrm{R}}x_{\mathrm{R}}(t) + B_{\mathrm{R}}e(t) & \text{if } e(t) \neq 0, \\ x_{\mathrm{R}}(t^+) = A_\rho x_{\mathrm{R}}(t) & \text{if } e(t) = 0, \\ u_{\mathrm{R}}(t) = C_{\mathrm{R}}x(t) + D_{\mathrm{R}}e(t), \end{cases} \tag{2-17}$$

with reset controller state vector $x_{\mathrm{R}} \in \mathbb{R}^{n_{\mathrm{R}}}$ with n_{R} states, time $t \in \mathbb{R}$ with $t^+ := \lim_{\tau \to 0^+} \tau$, resetting matrix A_ρ, and $A_{\mathrm{R}}, B_{\mathrm{R}}, C_{\mathrm{R}}, D_{\mathrm{R}}$ forming the state-space representation of the base linear system (BLS). The BLS is the dynamics that govern the system at all times *except* at reset instances. The resetting matrix determines the reset controller's states after a reset has occurred. All states are reset to zero, thus like with a CI element, if $A_\rho = [0]_{n_{\mathrm{R}} \times n_{\mathrm{R}}}$.

2-2-2 Performance prediction

The steady-state closed-loop performance of linear control systems can accurately be predicted using the sensitivity. However, obtaining a tool like the sensitivity is not as straightforward for nonlinear systems as it is for linear systems. The nonlinear nature a reset controllers as defined in (2-17) necessitates a different approach to be able to employ loop-shaping controller design for accurate closed-loop performance prediction. Guo *et al.* [6] introduced an analytical computation of the SIDF for reset controllers. This creates a link between open-loop and closed-loop behaviour, allowing for loop-shaping based on FRF data from the plant. However, as is generally the case for nonlinear systems, using the SIDF in loop-shaping design using the sensitivity inherently comes with inaccuracies due to the higher-order harmonics missed by the SIDF. This can result in significant deviations between predicted and achieved performance [18, 19]. This necessitates a more accurate description of the link between open-loop and closed-loop behaviour than the SIDF offers to obtain a more accurate performance prediction.

In 2021, Saikumar *et al.* developed a HOSIDF description [7] as an extension to the SIDF for reset controllers. Using HOSIDFs, Dastjerdi *et al.* formulated a method for closed-loop performance prediction utilising the pseudo-sensitivity [8, Definition 5]. This allows for a more accurate prediction than using the SIDF [7], decreasing the gap between predicted and achieved closed-loop performance using loop-shaping. The HOSIDF description currently only exists in literature for continuous-time RCSs in the form of (2-17).

Dastjerdi *et al.* [8, Definition 5] define the pseudo-sensitivity as the ratio between the computed, approximate error signal and amplitude of the reference signal of the RCS at each frequency. Three assumptions noted next underlie comput-

ing these approximate error signals [7]. The extent to which the assumptions are violated largely influences the accuracy of the approximate error signals and, indirectly, of the pseudo-sensitivity.

Assumption 1 | The RCS is input-to-state convergent in the sense defined in [7, Assumption 1].

Assumption 2 | A zero crossing of the error signal results in a state reset. Zero crossings occur $\pi/\omega_{\text{input}}$ apart, where ω_{input} is the input frequency causing the error signal. This spacing of the zero crossings results in two resets per priod of the input frequency.

Assumption 3 | Resets are only triggered by the first harmonic of the error. Hence, only the first harmonic of the error generates higher-order harmonics.

2-2-3 Stability

Literature on the closed-loop stability of FRF-based RCSs in the form of (2-17) for which a HOSIDF analysis is possible is fairly scarce. A prominent development towards proving the closed-loop stability of RCSs, proposed by Beker [4], is the H_β-condition. His theorem states that for a stable BLS, the RCS is quadratically stable if and only if the H_β-condition is satisfied. Dastjerdi *et al.* propose a method to prove the uniformly bounded-input bounded-state (UBIBS) property of several reset elements, namely first-order reset elements GFORE, CI and proportional Clegg integrator (PCI) [20, Theorem 2], and second-order reset elements generalised second-order reset element (GSORE) [20, Theorem 4] and second-order single-state reset elements (SOSRE) [20, Corollary 3]. The method utilises the Nyquist stability vector (NSV), which is based on the H_β-condition, although it does not require directly proving the H_β-condition. Additionally, the method is based on FRF data from the plant, thus a parametric model of the plant is not required.

The methods in [20] only provide a stability proof for specific reset elements, optionally with a linear pre- and post-filter. They do not provide a stability proof for RCSs containing parallel linear controller elements. Guo *et al.* found that for $A_\rho = \gamma \in \mathbb{R}$, stability of a reset element in open loop *at least* requires that $\gamma_i \in [-1, 1]$ [6, Proposition 2].

2-2-4 GFbI element

A GFbI element is a novel nonlinear integrator proposed by van Eijk *et al.* in 2024 (in press) [11]. Essentially, a GFbI element combines a PI element with a GFORE by placing them in series. A GFORE, similar to a CI element, provides reduced phase lag compared to a PI element at the cost of the generation of higher-order harmonics and possibly the emergence of limit cycles. The PI element C_{PI} is defined as

$$C_{\text{PI}}(s) = \frac{\omega_{\text{c}} + s}{\omega_{\text{c}} s}. \tag{2-18}$$

The GFORE is expressed in state space by (2-17) with

$$A_{\text{R}} = -\omega_{\text{r}}, \tag{2-19a}$$
$$B_{\text{R}} = \omega_{\text{r}}, \tag{2-19b}$$
$$C_{\text{R}} = 1, \tag{2-19c}$$
$$D_{\text{R}} = 0, \tag{2-19d}$$
$$A_\rho = \gamma, \tag{2-19e}$$

where integrator frequency $\omega_{\text{r}} \in \mathbb{R}_{>0}$. Due to the stability requirement in [6], $\gamma \in [-1, 1]$. Additionally, the GFORE's corner frequency is

$$\omega_{\text{r}} = \frac{\omega_{\text{c}}}{\sqrt{1 + \Theta_{\text{D},\infty}^2}}, \quad \Theta_{\text{D},\infty} = \frac{4(1-\gamma)}{\pi(1+\gamma)}. \tag{2-20}$$

Figure 2-5 shows the schematic representation of a GFbI element with integrator frequency $\omega_{\text{i}} \in \mathbb{R}_{\geq 0}$ placed in parallel with a proportional gain of 1 to obtain a proportional GFORE-based integrator (PGFbI) element. A PGFbI element can be used to replace a PI element.

In a GFbI element, the linear integral action of C_{PI} dominates up to around the phase-shift frequency $\omega_{\text{c}} \in \mathbb{R}_{>0}$. For higher frequencies, the nonlinear integral action of the GFORE dominates. Consequently, the phase shifts from -90 degrees to -38.1 degrees around ω_{c}. Generally, the phase only matters for stability and robustness in the middle-frequency region, which is where the bandwidth lives. The phase shift frequency can be tuned such that the frequency region where C_{PI}

dominates is maximised, whilst providing the reduced phase lag around the bandwidth and for frequencies above. This is illustrated in Figure 2-6.

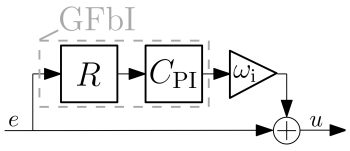

Figure 2-5: Schematic representation of a PGFbI [11].

For increasing ω_c, higher-order harmonics diminish as the nonlinearity of the GFbI is dominant for a decreasing frequency range. This observed favourable *frequency specificity*, allowing tuning of the frequency regions where linear and nonlinear behaviour in the RCS dominates, is what makes the GFbI element preferable over the only other alternative in its class, the PI+CI element.

The SIDF in general is accurate for linear systems. The more nonlinear behaviour a system shows, the more accuracy the SIDF loses. With regards to the GFbI element, this translates to accurate performance prediction for the system in the low-frequency region. For middle and especially higher frequencies, however, an SIDF analysis of the GFbI element still loses accuracy, resulting in degraded performance prediction. By using a HOSIDF analysis instead, accurate performance prediction is possible, paving the way for loop-shaping by means of the pseudo-sensitivity.

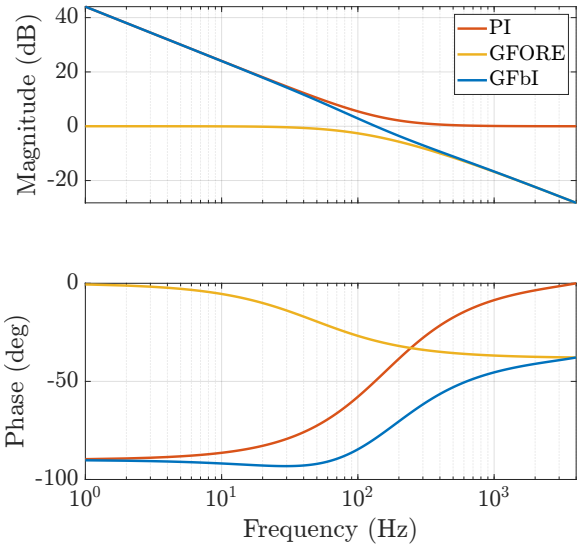

Figure 2-6: Magnitude and phase characteristics of the GFbI reset element and its constituents. The red line is $C_{\text{PI}}(s) \cdot 10^3$ given by (2-18) with $\omega_c = 10^3$. The yellow line is a GFORE with ω_r following from (2-20). The blue line is the GFbI, obtained by placing $C_{\text{PI}}(s) \cdot 10^3$ and the GFORE in series.

Chapter 3

GFbI controller sequences

For linear controllers, the order of the controller elements does not change the behaviour of the controller due to the principle of superposition [14, Chapter 5]. However, the principle of superposition does not hold for nonlinear systems, such as an RCS. The sequence of the controller elements can make a difference for RCSs, depending on what is changed. A key insight in this regards is the amplification of higher-order harmonics by a lead filter, which can be mitigated by placing the lead filter in parallel to the reset element. For an RCS containing a GFbI element, further called GFbI controller, two different sequences are compared. In the first considered sequence, the reset element and a lead filter are placed in series, where the output of the reset element is fed into the lead filter in open loop. This is further detailed in Section 3-1. In the second considered sequence, the reset element and lead filter are placed in parallel to prevent the output of the reset element from passing through the lead filter in open loop. This is discussed in Section 3-2. Finally, a generalised form for a GFbI controller of any sequence is given in Section 3-3. This generalised form is used to ensure the GFbI controller adheres to the performance prediction theorems discussed in Section 2-2-2, regardless of the controller element sequence.

3-1 Serial sequence base linear system

Linear controllers are often designed in a sequence where all controller elements are placed in series. Such a serial sequence of linear controller elements, further called a serial linear controller, is illustrated in Figure 3-1. The controller in Figure 3-1 contains controller elements that are commonly used in industry. The controller elements are a PI element with integrator frequency $\omega_{\mathrm{i,s}} \in \mathbb{R}_{\geq 0}$, a proportional gain $k_{\mathrm{P,s}} \in \mathbb{R}$, a lead-lag filter $C_{\mathrm{lead,s}}$ defined as

$$C_{\mathrm{lead,s}}(s) = s + k_{\mathrm{D,s}}, \tag{3-1}$$

with lead filter constant $k_{\mathrm{D,s}} \in \mathbb{R}$, a lag filter C_{lag} defined as

$$C_{\mathrm{lag}}(s) = \frac{1}{s + k_{\mathrm{T}}}, \tag{3-2}$$

with lag filter constant $k_{\mathrm{T}} \in \mathbb{R}$, and notch filters defined as

$$C_{\mathrm{notches}}(s) = C_{\mathrm{notch},1}(s) \cdot C_{\mathrm{notch},2}(s) \cdot \ldots \cdot C_{\mathrm{notch},n}(s), \tag{3-3}$$

where $n \in \mathbb{N}$ is the total number of notch filters and each notch filter is defined as

$$C_{\mathrm{notch}}(s) = \frac{s^2 + k_{m1} b_{m1} s + k_{m1}}{s^2 + k_{m2} b_{m2} s + k_{m2}}, \tag{3-4}$$

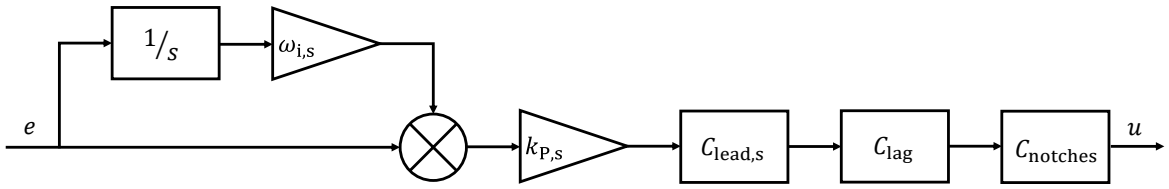

Figure 3-1: Schematic representation of a serial linear controller as seen in generic industrial applications.

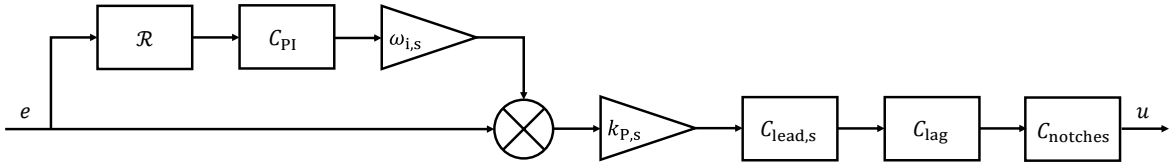

Figure 3-2: Schematic representation of a serial GFbI controller.

with skewed notch filter constants and damping coefficients $k_m \in \mathbb{R}$ and $b_m \in \mathbb{R}$, where subscript "m" denotes that the parameters corresponds to notch filter $m \in \{q \in \mathbb{N} | 1 \leq q \leq n\}$. Additionally, the additional subscript "$,\mathrm{s}$" denotes that the controller or parameter corresponds to a serial controller.

If the integrator of a serial linear controller is replaced by a GFbI element, a *serial GFbI controller* is obtained. The BLS of a serial GFbI controller is placed in a sequence such that all controller elements are in series. Applying the integrator replacement on the serial linear controller from Figure 3-1, a controller as illustrated in Figure 3-2 is obtained. The reset element $\mathcal{R}$ denotes the GFORE given in (2-19) and C_{PI} is the PI element given in (2-18). The other controller elements are the same as in the serial linear controller of Figure 3-1.

As shown in Figure 3-2, the PGFbI, proportional gain, $C_{\mathrm{lead,s}}$, C_{lag} and C_{notches} are all placed in series. The error is directly used as the input of the reset element. The output of the reset element proceeds to pass through all linear controller elements before entering the plant. As the reset element generates higher-order harmonics, these also pass through all linear controller elements. Of special interest is that the higher-order harmonics pass through $C_{\mathrm{lead,s}}$. The lead filter amplifies the higher-order harmonics in open loop, increasing the error. In closed loop, the amplified higher-order harmonics enter the lead filter once more and are amplified again, increasing the error even more. Whilst maintaining a serial sequence, the lead filter can be placed in before the reset element to prevent it from amplifying the higher-order harmonics. However, the lead filter then amplifies noise, which is fed to the input of the reset element, which may lead to an unnecessary increase in the number of resets. For this work, the focus is on sequences for which the input of the reset element is the direct error signal.

3-2 Parallel sequence base linear system

The controller elements of the controller shown in Figure 3-1 can be re-ordered such that the lead filter is placed in parallel with the integrator, as shown in Figure 3-3. Some of the parameters change when re-ordering the controller, namely

$$k_{\mathrm{P,p}} = \omega_{\mathrm{i,s}} + k_{\mathrm{D,s}}, \tag{3-5a}$$

$$\omega_{\mathrm{i,p}} = \omega_{\mathrm{i,s}} \cdot k_{\mathrm{D,s}}, \tag{3-5b}$$

$$k_{\mathrm{D,p}} = 1, \tag{3-5c}$$

with proportional gain $k_{\mathrm{P,p}} \in \mathbb{R}$ element, integrator frequency $\omega_{\mathrm{i,p}} \in \mathbb{R}_{\geq 0}$ and lead filter constant $k_{\mathrm{D,p}} \in \mathbb{R}$. The additional subscript "$,\mathrm{p}$" denotes the controller or parameter corresponds to a parallel controller. The lag filter is placed in all three parallel branches to ensure each branch as a whole can be expressed by a proper transfer function, which would otherwise not be the case for the branch containing the derivative action.

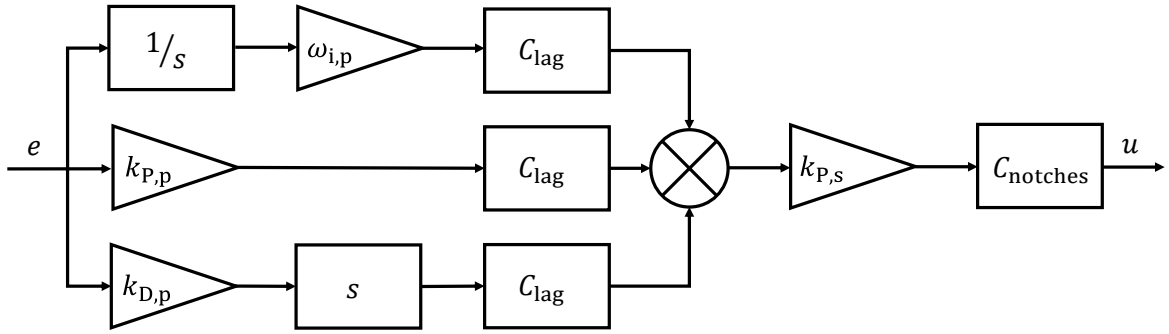

Figure 3-3: Schematic representation of a parallel linear controller. This is equivalent to the serial linear controller in Figure 3-1.

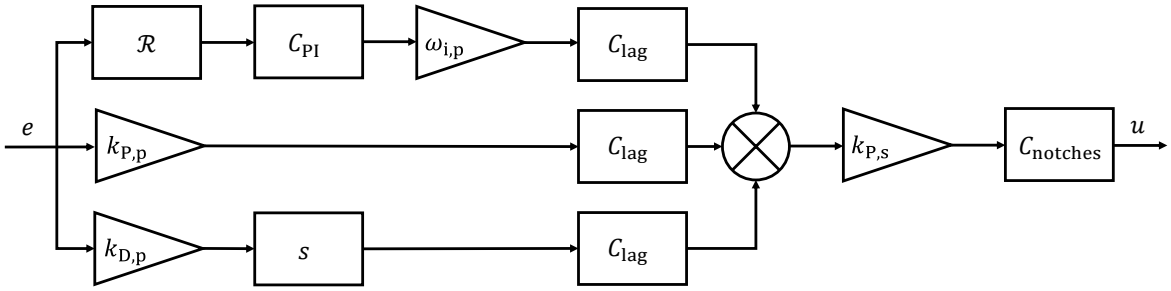

Figure 3-4: Schematic representation of a parallel GFbI controller.

Similarly to the serial linear controller, the integrator of a parallel linear controller can be replaced by a GFbI element to obtain a *parallel GFbI controller*. The BLS of a parallel GFbI controller is placed in a sequence such that the GFbI element and derivative action are in parallel. Applying the integrator replacement on the parallel linear controller from Figure 3-3, a controller as illustrated in Figure 3-4 is obtained. The reset element $\mathcal{R}$ denotes the GFORE given in (2-19) and C_{PI} is the PI element given in (2-18). The lead filter of the serial GFbI controller is now separated in its proportional gain and derivative action, as the proportional gain is combined with the proportional gain of the PGFbI element. The other controller elements are the same as in the parallel linear controller of Figure 3-3.

By placing the reset element in parallel with the derivative action, the output of the reset element does not pass through the derivative action in open loop. Therefore, the derivative action does not amplify the higher-order harmonics generated by the reset element in open loop. After passing through the closed loop once, the higher-order harmonics enter the derivative action once, increasing the error. Compared to a serial GFbI controller, where the higher-order harmonics pass through the lead filter both in open loop and in closed loop, a parallel GFbI controller amplifies the higher-order harmonics less, resulting in a lesser increase of the error. The integrating action, along with the advantages thereof compared to a linear PI element, remains the same in both a serial and parallel GFbI controller.

3-3 Generalised sequence base linear system

Any GFbI controller, whether it has a serial, parallel, or any other controller element sequence, can be transformed to the equivalent generalised form shown in Figure 3-5 with the reset element $\mathcal{R}$ denoting the GFORE given in (2-19). Due to the principle of superposition [14, Chapter 5], the linear controller elements in series and in parallel with

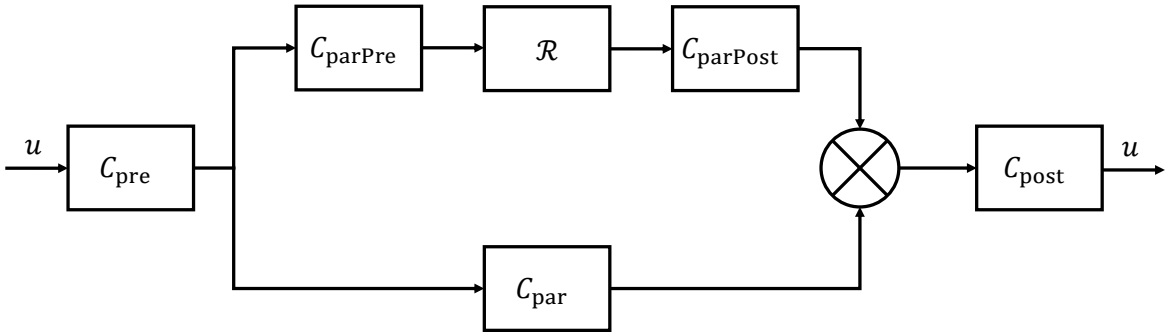

Figure 3-5: Generalised sequence reset controller architecture.

the reset element can be combined such that the resulting controller is equivalent to the original controller.

The purpose of transforming the GFbI controllers is to ensure the RCS adheres to the form used in performance prediction theorems discussed in Section 2-2-2. Additionally, the generalised form introduces as little discretisation inaccuracies as possible, as detailed in Section 4-1-1.

Furthermore, to be able to compute the output signal of the lead filter in a serial GFbI controller or the derivative action in a parallel GFbI controller, those controller elements need to be combined with another controller element to make the resulting combined controller element proper. This is achieved for both GFbI controllers by transforming them to the generalised form shown in Figure 3-5.

Chapter 4

GFbI feedback autotuner

Consider any control system using a linear feedback controller that adheres to the constraints imposed on the system, if any are present. Let the system of the plant controlled by the linear feedback controller be called the *reference linear system* and let the performance of the reference linear system be denoted as the *linear performance*, which is measured by frequency-domain performance prediction metrics. Also consider a GFbI controller with the same controller elements as the reference linear system as its BLS except for the integrator, and let the performance of the system with the same plant controlled by the GFbI controller be denoted as the *nonlinear performance*, which is measured by the same frequency-domain performance prediction metrics as the linear performance. By changing the parameters of the GFbI controller, namely its BLS and GFbI element, the nonlinear performance can be altered. Note that the BLS of the GFbI controller is changed, not the reference linear system. The nonlinear performance is compared to the linear performance from the reference linear system.

Tuning the GFbI controller is a rather complex and tedious task. Multiple parameters need to be optimised simultaneously that all strongly affect each other in non-intuitive ways. It is possible to formulate an objective function for this problem that, by design, steers towards a holistically optimal controller while capturing the interrelated effects of all parameters at once. Global optimisation algorithms are well suited for this kind of complex and tedious problems for which such an objective function can be conceived.

The GFbI feedback autotuner (GFA) is an optimisation algorithm that iteratively attempts to find holistically optimal parameters for the GFbI controller using the described objective function to ensure the nonlinear performance is better than the linear performance. In each iteration, a candidate GFbI controller is synthesised with a new set of parameters. For each candidate GFbI controller, it is verified whether the constraints are satisfied and how well the candidate GFbI controller performs with respect to the GFA's optimisation target. After the algorithm finishes, the set of parameters that resulted in the best performing GFbI controller forms the optimal solution.

This chapter presents the GFA, along with the necessary details required to understand how the GFA works. First, the assumptions the GFA is based on are provided in Section 4-1. Subsequently, the types of constraints that the GFA can impose on a GFbI controller are given in Section 4-2, followed by the optimisation target in Section 4-3. Finally, Section 4-4 elaborates on how all constraints and the optimisation target are combined to design a tuned GFbI controller.

4-1 Internal mechanics

This section elaborates on some internal mechanics that are relevant for various certain processes in the GFA. First, Section 4-1-1 discusses the discretisation of GFbI controllers and the effects thereof on performance prediction accuracy. Subsequently, to verify assumption 2, a method is needed to determine the number of resets per period of the input frequency. Details on how this can be done are given in Section 4-1-2. Lastly, as a GFbI element contains both linear and nonlinear behaviour, a decision needs to be made on how much nonlinearity can be added to the system and why. Section 4-1-3 details how the amount of nonlinearity can be optimised and what assumptions are involved.

4-1-1 Controller discretisation

A GFbI controller is implemented in an RCS in discrete time. Before discretisation, the GFbI controller is transformed to the generalised form shown in Figure 3-5. The generalised form minimises the number of discretisations, along with the inaccuracies introduced thereby, by minimising the number of linear controller elements. This minimises the inaccuracy caused by the number of discretisations. All linear controller elements are discretised using the Tustin approximation, as this discretisation method generally yields the smallest discretisation error [21].

The BLS of the GFORE is also discretised using the Tustin approximation. The discrete GFORE is implemented digitally as

$$\mathcal{R}_d = \begin{cases} x_{\mathrm{R}}(k+1) = -\omega_{\mathrm{r}} x_{\mathrm{R}}(k) + \omega_{\mathrm{r}} e(k) & \text{if } \delta_e(k) > 0, \\ x_{\mathrm{R}}(k+1) = \gamma x_{\mathrm{R}}(k) & \text{if } \delta_e(k) \leq 0, \\ u_{\mathrm{R}}(k) = x(k), \end{cases} \tag{4-1}$$

where $\mathcal{R}_d$ is the discrete GFORE with time step $k \in \mathbb{Z}$ and zero-crossing-detection variable $\delta_e(k)$, defined as

$$\delta_e(k) = e(k) \cdot e(k-1), \tag{4-2}$$

where $e(k-1) = 0 \,|\, k = 0$.

Analytical performance prediction has currently only been developed for continuous-time RCSs. However, as the GFbI controller is implemented in discrete time, the performance prediction is performed with FRFs obtained from the discretised controllers. An FRF of the GFORE is obtained using the theory from [7, 8]. For the GFA, the inaccuracy of the continuous-time performance prediction theory performed with discrete time data is assumed negligible. Moreover, to the best of the author's knowledge, there is currently no alternative to perform performance prediction for the GFA.

4-1-2 Number of resets

Assumption 2 must be verified for each individual frequency at which the pseudo-sensitivity is computed. Hence, a method is needed to determine the number of resets per period of the input frequency.

Following [7], the error signal at a specific frequency can be computed for one period of the input frequency while taking the HOSIDFs into account. This is done in discrete time with a finite sampling period $T_{\mathrm{s}} \in \mathbb{R}_{>0}$. With this error signal, the number of zero crossings can be counted. The number of resets for a specific frequency, denoted by $N_{\mathrm{r}}(\omega)$, is equal to the number of zero crossings in the error signal at that frequency. Assumption 2 holds if $N_{\mathrm{r}}(\omega) = 2$ and does not hold if $N_{\mathrm{r}}(\omega) \neq 2$.

Since the error signal is computed in discrete time instants, one period of the input frequency is not necessarily equal to an integer multiple of T_{s}. This results in the error signal being either truncated before or extended after exactly one period of the input frequency. From here on, it is assumed that the truncation method is used. For a truncated error signal, one zero crossing may be missed. This is illustrated in Figure 4-1. It is known that the error signal should be connected at the start and end for one period of the input frequency, indicated by the dotted line. Since the sinusoidal input $\sin(t\,\omega_{\mathrm{input}})$ is an odd function, the even higher-order harmonics in the error signal are zero [7]. Hence, the number of resets for one period of the input frequency must be even. From this, it can be concluded that if the detected number of zero crossings is odd, one zero crossing was missed. The number of resets then equals the number of detected zero crossings plus one.

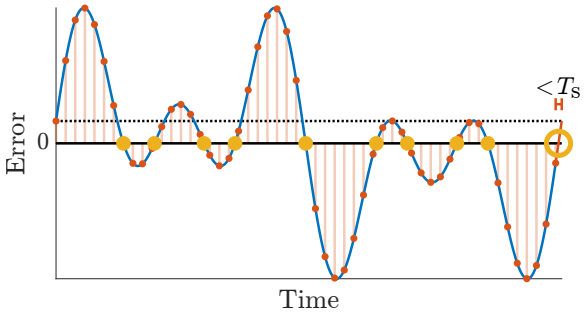

Figure 4-1: One zero crossing is not detected due to truncation of the error signal over one period of the input frequency. The red dots indicate sampling points taken at a sampling period of T_s. The red signal at the end of the blue signal indicates the truncated end of the error signal, which is inherently shorter than one sampling period. The solid yellow dots mark detectable zero crossings, whereas the unfilled circle marks an undetectable zero crossing.

Whether assumption 2 holds for a range of frequencies can be encapsulated in a single variable. Since $\sin(t\,\omega_{\text{input}})$ is an odd periodic function, $N_r(\omega) \geq 2\ \forall \omega \in (0, \infty)$. For all frequencies between any $\omega_1, \omega_2 \in \bar{\mathbb{R}}_{>0}$ with $\omega_1 < \omega_2$, the maximum N_r among all corresponding error signals is defined as

$$M_r(\omega_1, \omega_2) = \max_{\omega \in [\omega_1, \omega_2]} N_r(\omega). \tag{4-3}$$

For $\omega \in [\omega_1, \omega_2]$, assumption 2 holds if $M_r(\omega_1, \omega_2) = 2$ and does not hold if $M_r(\omega_1, \omega_2) \neq 2$.

4-1-3 Nonlinearity optimisation

The phase shift frequency ω_c determines from which frequency range the GFORE dominates over the PI element in a GFbI element, along with the corresponding decrease in phase lag. Therefore, ω_c effectively determines the amount of nonlinearity a GFbI element exhibits. For decreasing ω_c, nonlinear behaviour in the GFbI dominates for a larger range of frequencies, and vice versa for increasing ω_c.

Consider a discrete RCS and let ω_N denote the Nyquist frequency. Additionally, let $\omega_1, \omega_2 \in (0, \omega_N]$ and $\omega_1 < \omega_2$. A GFbI roughly has linear behaviour for all $\omega < \omega_c$ due to the PI element dominating there and nonlinear behaviour for all $\omega > \omega_c$ due to the GFORE dominating there. Between any $\omega \in (0, \omega_N]$, as many higher-order harmonics can be computed that contribute to the error signal as can be sampled between ω and ω_N according to the Nyquist criterion. As the frequency range between a low frequency and ω_N is larger than the frequency range between a high frequency and ω_N, a low frequency has more higher-order harmonics contributing to the error signal than a high frequency. These higher-order harmonics can cause $N_r(\omega) \neq 2$. Thus, a low frequency has more higher-order harmonics contributing to the error that can cause $N_r(\omega) \neq 2$ than a high frequency. Moreover, for increasing nonlinearity by decreasing ω_c, for any frequency range $\omega \in [\omega_1, \omega_2]$, the frequency range for which $N_r(\omega) \neq 2$ will grow from ω_1 to ω_2 and the total number of frequencies for which $N_r(\omega) \neq 2$ will monotonously increase. Thus, by changing ω_c, the frequency below which $N_r(\omega) \neq 2$ and above which $N_r(\omega) = 2$ can be changed. This frequency at which $N_r(\omega)$ changes from $\neq 2$ to $= 2$ is denoted by $\omega_{\text{skip}} \in \mathbb{R}_{>0}$ and is defined as

$$N_r(\omega) \neq 2\ \forall \omega \in (0, \omega_{\text{skip}}) \tag{4-4a}$$
$$N_r(\omega) = 2\ \forall \omega \in [\omega_{\text{skip}}, \omega_N], \tag{4-4b}$$

where (4-4b) is limited to the Nyquist frequency as N_r can only be computed up to that frequency. It was observed that for increasing nonlinearity by decreasing ω_c, ω_{skip} monotonously increases. The definition of ω_{skip} in (4-4) logically requires that for any two frequencies $\omega_1, \omega_2 \in (0, \omega_N]$,

$$\nexists\, \omega_1 < \omega_2 \ni \begin{cases} N_r(\omega_1) = 2, \\ N_r(\omega_2) \neq 2, \end{cases} \tag{4-5}$$

which is assumed to hold.

To obtain as much phase advantage as possible from the use of a GFbI element, the nonlinearity is to be maximised. This is achieved by minimising ω_c as much as possible. However, decreasing ω_c also increases ω_{skip}, leading to assumption 2 not holding for a larger range of frequencies. A key insight is that it may not be necessary for assumption 2 to hold for all frequencies. If there are frequencies at which the pseudo-sensitivity is not

needed, assumption 2 may be safely violated at those frequencies, allowing for more nonlinearity to enter the control system to improve the control system's performance. An optimal value for ω_c can be found by inverting its relation with ω_{skip}, hence making ω_{skip} the tuneable design variable. Then, ω_c is determined through ω_{skip} by selecting a desired ω_{skip} and iteratively optimising ω_c until (4-4) holds.

The value of ω_{skip} is chosen such that

$$|S_{linear}(\omega_{skip})| = S_{skip}, \tag{4-6}$$

where $S_{linear}(\omega_{skip})$ is the sensitivity of the reference linear system at ω_{skip} and $S_{skip} \in \bar{\mathbb{R}}$ is the value for the sensitivity and pseudo-sensitivity below which the error is suppressed to such a degree that it can be considered negligible. The value of S_{skip} may vary for each use case and is chosen by the control system designer. If the pseudo-sensitivity is required to be valid for all frequencies, S_{skip} is chosen as $S_{skip} = -\infty$.

Assumption 2 does not hold for any $\omega < \omega_{skip}$ and thus the pseudo-sensitivity is not valid at those frequencies. Hence, it cannot be verified whether the pseudo-sensitivity for any $\omega < \omega_{skip}$ is below S_{skip}. However, it is assumed that the suppression of the error at those frequencies by the GFbI controller remains below S_{skip}.

Optimisation of ω_c such that (4-4) holds for a chosen ω_{skip} is done using a bisection algorithm. Assume a GFbI controller where all of its controller element parameters are constant except for the value of ω_c of the GFbI element. Let

$$M_r^\star(\omega_c) = M_r(\omega_{skip}, \omega_N), \tag{4-7}$$

where M_r is computed using the GFbI controller with the value of ω_c equal to the input of $M_r^\star$. The bisection algorithm starts with a lower bound $\omega_{lb} \in \mathbb{R}_{>0}$ with $M_r^\star(\omega_{lb}) \neq 2$ and an upper bound $\omega_{ub} \in \mathbb{R}_{>0}$ with $M_r^\star(\omega_{ub}) = 2$. The bounds are chosen by the control system designer, who has to ensure the $M_r^\star$ condition of both bounds hold. The $M_r^\star$ conditions guarantee the optimal ω_c lies between the bounds. In each iteration of the bisection algorithm, $M_r^\star(\omega_{mid})$ is computed with $\omega_{mid} = (\omega_{lb} + \omega_{ub})/2$. Subsequently, one of the bounds is replaced by ω_{mid}. Which bound is replaced is determined by

$$\omega_{lb} \leftarrow \omega_{mid} \quad \text{if } M_r^\star(\omega_{mid}) \neq 2, \tag{4-8a}$$
$$\omega_{ub} \leftarrow \omega_{mid} \quad \text{if } M_r^\star(\omega_{mid}) = 2, \tag{4-8b}$$

where $\leftarrow$ denotes the value of the left variable is replaced by the value of the right variable. The bisection iterations are continued until ω_{mid} converges to within a tolerance, denoted by $\omega_{tol} \in \mathbb{R}_{>0}$. The tolerance is chosen by the control system designer.

As the GFA varies parameters of the GFbI controller in each iteration, the ω_{lb} and ω_{ub} required such that $M_r^\star(\omega_{lb}) \neq 2$ and $M_r^\star(\omega_{ub}) = 2$ varies. The control system designer could choose ω_{lb} and ω_{ub} sufficiently low and high, respectively, such that for all candidate GFbI controllers the GFA can design, $M_r^\star(\omega_{lb}) \neq 2$ and $M_r^\star(\omega_{ub}) = 2$ can reasonably be expected to hold. However, this can be expected to lead to a larger or at best equal number of iterations for ω_c optimisation for *most* candidate GFbI controllers than if ω_{lb} and ω_{ub} were closer together, with the resulting computational cost.

The GFA has a bound expansion mechanism to change ω_{lb} and ω_{ub} if $M_r^\star(\omega_{lb}) \neq 2$ or $M_r^\star(\omega_{ub}) = 2$ does not hold for a candidate GFbI controller. Before computing $M_r^\star(\omega_{mid})$ for the first time, $M_r^\star(\omega_{lb})$ and $M_r^\star(\omega_{ub})$ are computed. If either $M_r^\star(\omega_{lb}) \neq 2$ or $M_r^\star(\omega_{ub}) = 2$ does not hold, the condition-violating bound is either divided or doubled by a factor $f_{exp} \in (1, \infty)$, depending on whether it concerns ω_{lb} or ω_{ub}. This bound expansion mechanism can be denoted as

$$\omega_{lb} \leftarrow \frac{\omega_{lb}}{f_{exp}} \quad \text{if } M_r^\star(\omega_{lb}) = 2, \tag{4-9a}$$
$$\omega_{ub} \leftarrow f_{exp} \cdot \omega_{ub} \quad \text{if } M_r^\star(\omega_{ub}) \neq 2. \tag{4-9b}$$

Equation (4-9) is repeated until both $M_r^\star(\omega_{lb}) \neq 2$ and $M_r^\star(\omega_{ub}) = 2$ hold or until one of the bounds is expanded up to n_{exp} times. A suitable n_{exp} is chosen by the control system designer. Every time a bound is expanded, the other bound can be moved to the former value of the expanded bound to decrease the iterations required for convergence of the bisection algorithm. For example, if a lower bound is found to have $M_r^\star(\omega_{lb}) = 2$, this value of ω_{lb} is suitable as a new upper bound, as it satisfied the criterion of $M_r^\star(\omega_{ub}) = 2$. Thus, the lower

bound is expanded according to (4-9a), and additionally, the value of the upper bound is assigned the value of the former lower bound. This can be denoted as

$$\omega_{\text{ub}} \leftarrow \omega_{\text{lb}} \qquad \text{if } M_{\text{r}}^{\star}(\omega_{\text{lb}}) = 2, \tag{4-10a}$$

$$\omega_{\text{lb}} \leftarrow \omega_{\text{ub}} \qquad \text{if } M_{\text{r}}^{\star}(\omega_{\text{ub}}) \neq 2. \tag{4-10b}$$

In the example case, (4-10a) applied.

After suitable bounds have been found, $M_{\text{r}}^{\star}(\omega_{\text{mid}})$ is computed and the bisection algorithm continues as described. If no ω_{lb} can be found after n_{exp} expansions such that $M_{\text{r}}^{\star}(\omega_{\text{lb}}) \neq 2$, the GFA continues with the lowest ω_{lb} it found as ω_{c}. In this case, assumption 2 holds for the candidate GFbI controller. If no ω_{ub} can be found after n_{exp} expansions such that $M_{\text{r}}^{\star}(\omega_{\text{ub}}) = 2$, the GFA continues with the highest ω_{lb} it found as ω_{c}. In this case, assumption 2 does not hold for the candidate GFbI controller.

The bound expansion mechanism gives the control system designer the freedom to select a ω_{lb} and ω_{ub} such that not all candidate GFbI controllers necessarily have to adhere to $M_{\text{r}}^{\star}(\omega_{\text{lb}}) \neq 2$ and $M_{\text{r}}^{\star}(\omega_{\text{ub}}) = 2$ for the initial ω_{lb} and ω_{ub}. This can reduce the computational cost of optimising ω_{c}. For some candidate GFbI controllers, the computational cost is lower, as less ω_{c} bisection algorithm iterations are needed for convergence of ω_{c}. However, for some candidate GFbI controllers, the computational cost is higher due to first expanding the bounds and only then executing the bisection algorithm. Whether the savings in computational cost of the ω_{c} bisection algorithm iterations by selecting ω_{lb} and ω_{ub} closer together outweighs the added computational cost of expanding the bounds when required and checking the initial bounds for every candidate GFbI controller is at the discretion of the control system designer.

4-2 Constraints

The GFA can impose several types of constraints on the GFbI controller it optimises. All constraints are implemented in the same manner, where the violation of the constraint is transformed into a single metric that is used to compute the associated cost for the objective function. This is further detailed in Section 4-2-1.

The first two constraint types are open-loop constraints and pseudo-sensitivity constraints discussed in Sections 4-2-2 and 4-2-3, respectively. Multiple open-loop and pseudo-sensitivity constraints can be imposed on a GFbI controller where each constraint has a specified frequency range for which it is active. How many and for which frequency ranges any open-loop and pseudo-sensitivity constraints are needed depends on the use case and is at the discretion of the control system designer.

The third constraint type is a constraint on the number of resets per period of the input frequency and is discussed in Section 4-2-4. This constraint ensures that assumption 2 holds for all $\omega \in [\omega_{\text{skip}}, \infty)$. This constraint exists in the GFA only once, as there is nothing to vary for this constraint. As such, there are no parameters specifically for this constraint that need to be chosen by the control system designer.

The fourth and final constraint type is a constraint forcing the pseudo-sensitivity to be lower or equal to the sensitivity of the reference linear system for a specific frequency range and is discussed in Section 4-2-5. This constraint ensures the GFbI controller performs at least equally well in terms of sensitivity performance metrics for the specific frequency range. This frequency range cannot be determined by the control system designer, but rather is based on the performance of the reference linear system.

4-2-1 Constraint implementation

All constraints are modelled as a cost source that yields a high cost, namely in the order of magnitude of 10^6, when the constraint is violated and yields a cost of zero when the constraint is not violated. The extent to which a constraint is violated is captured in a single metric called the violation, denoted by $v_{\text{con}} \in \mathbb{R}$. Generally, v_{con} is in the order of magnitude of 10^0. How the violation is measured differs per constraint and is further detailed in Sections 4-2-2 to 4-2-5. For a violated constraint, the cost is linearly proportional to the violation. The cost is defined as

$$c_{\text{con}} = 0 \qquad \text{if } v_{\text{con}} \leq 0, \tag{4-11a}$$

$$c_{\text{con}} = \left(10^3 + v_{\text{con}}\right) \cdot 10^3 \qquad \text{if } v_{\text{con}} > 0. \tag{4-11b}$$

Equation (4-11) is qualitatively visualised in Figure 4-2.

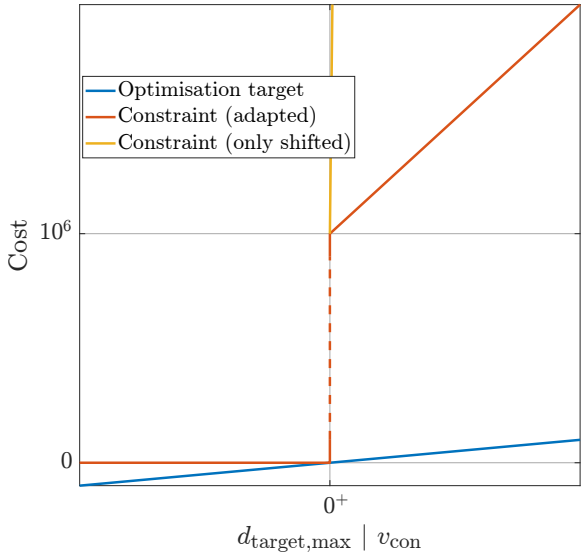

Figure 4-2: A qualitative visual representation of the optimisation target cost and the constraint cost. 0^+ denotes a point infinitesimally greater than zero. The visual representation of the constraint cost given in (4-11) is adapted for convenience of interpretation. The constraint cost, as represented by the red line, is visually shifted down and the inclination is reduced, indicated by the dashed line. The yellow line represents the shifted-down constraint cost with an unaltered inclination. The constraint cost exhibits a significantly larger inclination compared to the rejection target cost.

The constraint costs have a slope that decreases towards not violating the constraints to give the GFA a sense of direction. The slope is inclined in such a way that multiple weakly violated constraints exceed the cost of a single strongly violated constraint. This ensures that the GFA favours not violating a constraint over only reducing, but not preventing the violation of, one or several constraints.

4-2-2 Open-loop constraint

The GFA can impose any number of constraints on the open loop of the GFbI controller. Each constraint can be imposed on either all $\omega \in [\omega_{\text{skip}}, \omega_{\text{N}}]$ or a subset thereof. Let $\left[\omega_{L_{\text{low}}}, \omega_{L_{\text{high}}}\right] \subseteq [\omega_{\text{skip}}, \omega_{\text{N}}]$ be the frequency range on which an open-loop constraint is imposed. The open-loop constraint is defined as

$$M_{L_{\text{con}}} \leq L_{\text{lim,con}}, \tag{4-12}$$

with open-loop gain limit $L_{\text{lim,con}} \in \bar{\mathbb{R}}$ and

$$M_{L_{\text{con}}} = \max_{\omega \in \left[\omega_{L_{\text{low}}}, \omega_{L_{\text{high}}}\right]} |L(j\omega)|. \tag{4-13}$$

The violation of the open-loop constraint is obtained as

$$v_{\text{con}} = M_{L_{\text{con}}} - L_{\text{lim,con}}. \tag{4-14}$$

The cost associated with the constraint then follows from (4-11).

To outline, the parameters that are unique to each open-loop constraint that need to be chosen by the control system designer are $\omega_{L_{\text{low}}}$, $\omega_{L_{\text{high}}}$ and $L_{\text{lim,con}}$.

4-2-3 Pseudo-sensitivity constraint

The GFA can impose any number of constraints on the pseudo-sensitivity of the GFbI controller. Each constraint can be imposed on either all $\omega \in [\omega_{\text{skip}}, \omega_{\text{N}}]$ or a subset thereof. Let $\left[\omega_{S_{\text{low}}}, \omega_{S_{\text{high}}}\right] \subseteq [\omega_{\text{skip}}, \omega_{\text{N}}]$ be the frequency range on which a pseudo-sensitivity constraint is imposed. The pseudo-sensitivity constraint is defined as

$$M_{S_{\text{con}}} \leq S_{\text{lim,con}}, \tag{4-15}$$

with pseudo-sensitivity limit $S_{\text{lim,con}}$ and

$$M_{S_{\text{con}}} = \max_{\omega \in \left[\omega_{S_{\text{low}}}, \omega_{S_{\text{high}}}\right]} S_{\infty}(\omega), \tag{4-16}$$

where S_{∞} is the pseudo-sensitivity.

The violation of the pseudo-sensitivity constraint is obtained as

$$v_{\text{con}} = M_{S_{\text{con}}} - S_{\text{lim,con}}. \tag{4-17}$$

The cost associated with the constraint then follows from (4-11).

To outline, the parameters that are unique to each pseudo-sensitivity constraint that need to be chosen by the control system designer are $\omega_{S_{\text{low}}}$, $\omega_{S_{\text{high}}}$ and $S_{\text{lim,con}}$.

4-2-4 Number of resets constraint

As the GFbI controller is implemented in discrete time, the maximum frequency at which the pseudo-sensitivity can be computed is limited by the Nyquist criterion. The frequency range for which the pseudo-sensitivity is of interest is $\omega \in [\omega_{\text{skip}}, \omega_{\text{N}}]$. If assumption 2 does not hold for any $\omega \in [\omega_{\text{skip}}, \omega_{\text{N}}]$, the pseudo-sensitivity can not be used at that or those frequencies and frequency-domain performance prediction is not possible there. As frequency-domain performance prediction is the metric by which the GFA optimises the GFbI controller, it is needed for assumption 2 to hold for all $\omega \in [\omega_{\text{skip}}, \omega_{\text{N}}]$. The number of resets constraint ensures assumption 2 holds for all $\omega \in [\omega_{\text{skip}}, \omega_{\text{N}}]$. Note that assumption 2 holding is a necessary but not sufficient condition to use the pseudo-sensitivity, as there are two additional assumptions.

Assumption 2 holds for all $\omega \in [\omega_{\text{skip}}, \omega_{\text{N}}]$ if

$$N_{\text{r}}(\omega) = 2 \; \forall \omega \in [\omega_{\text{skip}}, \omega_{\text{N}}]. \tag{4-18}$$

Equation (4-18) is thus the number of reset constraint.

The nonlinearity is optimised by optimising ω_{c} for every candidate GFbI controller as further detailed in Section 4-1-3. It is possible the nonlinearity optimisation algorithm is unable to find an ω_{c} such that (4-18) holds for a candidate GFbI controller. In that case, as the GFbI controller is implemented in discrete time, there exists an integer number of frequencies for which $N_{\text{r}}(\omega) \neq 2$ for $\omega \in [\omega_{\text{skip}}, \omega_{\text{N}}]$. This integer number is denoted by $n_{\neq 2}$.

As further detailed in Section 4-1-3, for increasing nonlinearity and provided other parameters are constant, $n_{\neq 2}$ monotonously increases. This phenomenon is used to provide a slope to the cost of this constraint. The violation of the number of resets constraint is obtained from $n_{\neq 2}$ as

$$v_{\text{con}} = n_{\neq 2}. \tag{4-19}$$

As there is nothing to vary for this constraint, the control system designer does not need to choose any parameters.

4-2-5 Tracking constraint

The tracking constraint ensures the nonlinear performance is at least equal to the linear performance for a specific frequency range. This specific frequency range is from ω_{skip} up to the smallest frequency at which the linear sensitivity crosses 0 dB, denoted by ω_{track}. This frequency is mathematically denoted as

$$\omega_{\text{track}} = \min \omega \ni |S_{\text{linear}}(j\omega)| = 0 \text{ dB}. \tag{4-20}$$

The constraint is then denoted as

$$S_{\infty}(\omega) \leq |S_{\text{linear}}| \; \forall \omega \in [\omega_{\text{skip}}, \omega_{\text{track}}]. \tag{4-21}$$

The violation of the tracking constraint is obtained as

$$v_{\text{con}} = \max_{\omega \in [\omega_{\text{skip}}, \omega_{\text{track}}]} \left(S_{\infty}(\omega) - |S_{\text{linear}}(j\omega)| \right). \tag{4-22}$$

With this definition for the violation of the tracking constraint, the sensitivity of the reference linear system functions as a weight for the pseudo-sensitivity of the GFbI controller.

As there is nothing to vary for this constraint, the control system designer does not need to choose any parameters.

4-3 Optimisation target

The optimisation target provides a means for the GFA to suppress specific vibrations observed in the error. How well the specific vibrations are suppressed is transformed into a cost for the objective function. One or multiple frequency ranges can be specified by the control system designer to suppress in the pseudo-sensitivity. Similar to the tracking constraint, the sensitivity of the reference linear system functions as a weight for the pseudo-sensitivity of the GFbI controller.

For any targeted frequency region $n \in \mathbb{N}$, the difference between the reference linear system's sensitivity and the pseudo-sensitivity is denoted as

$$d_{\text{target},n}(\omega) = S_{\infty}(\omega) - |S_{\text{linear}}(j\omega)| \quad \forall \omega \in [\omega_{\text{start},n}, \omega_{\text{end},n}], \tag{4-23}$$

where $\omega_{\text{start},n}$ and $\omega_{\text{end},n}$ are the start and end frequencies of frequency region n, respectively. The

maximum $d_{\text{target},n}(\omega)$ across all regions is denoted as

$$d_{\text{target,max}} = \max_{n,\omega} \left(d_{\text{target},n}(\omega) \right). \tag{4-24}$$

The optimisation target is modelled as a cost source that yields a cost directly proportional to the worst $d_{\text{target,max}}$, namely as

$$c_{\text{target}} = d_{\text{target,max}} \tag{4-25}$$

The cost of the optimisation target, generally in the order of magnitude of 10^0, is negligible compared to the cost of a violated constraint, as qualitatively illustrated in Figure 4-2. This ensures the GFA prioritises the constraints over the optimisation target. Additionally, the inclination of the optimisation target cost is significantly less than that of a violated constraint. This ensures the GFA does not have a local minimum where the optimisation target is optimised whilst one or multiple constraints remain violated.

To outline, the parameters that are unique to the optimisation target that need to be chosen by the control system designer are $\omega_{\text{start},n}$ and $\omega_{\text{end},n}$ for each targeted frequency region.

4-4 GFA structure

This section describes how the GFA iteratively tunes a GFbI controller using a hybrid optimisation approach. Firstly, the general optimisation approach is given in Section 4-4-1. Secondly, Section 4-4-2 explains what parameters the GFA optimises and why. Thirdly, Section 4-4-3 describes how all cost sources are combined into the objective function. Finally, Section 4-4-4 provides additional details on the optimisation algorithms used, followed by an overview of the options used for each optimisation algorithm in Section 4-4-5, such as tolerances.

4-4-1 Hybrid optimisation approach

The GFA employs hybrid optimisation [22]. In a hybrid optimisation scheme, a global optimisation algorithm first finds a rough estimate of the global optimum. Subsequently, a local optimisation algorithm further searches for the local optimum starting from the rough global optimum the global optimisation algorithm found. In this scheme, the strength of both the global and local optimisation algorithms are utilised. The global optimisation algorithm is generally best at finding a solution living in the globally optimal basin of attraction, whereas the local optimisation algorithm is generally best at finding an accurate solution within a given basin of attraction. The local optimisation algorithm running after a global optimisation algorithm is called a hybrid function.

One run of the GFA consists of running four global optimisation algorithms consecutively. These are `particle swarm` [23], `genetic algorithm` [24], `surrogate optimisation` [25] and `simulated annealing` [26]. The algorithms run in the stated order. After each run of an algorithm, the hybrid function `pattern search` [27] runs once, starting from the best point the global optimisation algorithm found. After running the final hybrid function, the final solution of the GFA is obtained. All five optimisation algorithms are implemented using MATLAB.

These four global optimisation algorithms were chosen for their different approach to finding the global optimum. Using all four algorithms instead of using only one ensures a thorough search through the design space for the GFbI controller.

The objective function is nonsmooth. For nonsmooth optimisation problems, the local optimisation algorithm `pattern search` is well suited [22].

4-4-2 Objective function parameters

To GFA finds an optimal GFbI controller by tuning the parameters of the BLS and the GFbI element. The BLS has the same controller elements as the reference linear system, except for that the linear integrator is replaced by a GFbI element. Not all parameters of the BLS are necessarily optimised. If a subset of the BLS parameters are included as optimisation parameters, those not included are kept at the value they have in the reference linear controller. Of the GFbI element, only γ is included as an optimisation parameter, as ω_c is optimised internally for every candidate GFbI controller. It

was tested whether including ω_c as an optimisation parameter produced better results than optimising ω_c internally. However, the GFA produced a similar result, whilst the runtime of the GFA was increased considerably. The optimisation parameters are assigned bounds for the optimisation, as all algorithms generally work faster with bounds due to having to explore a smaller design space. Additionally, `surrogate optimisation` requires the use of bounds on the optimisation parameters.

There is a caveat in exploring the design space with the chosen optimisation parameters. The GFA does not test for the stability of any candidate GFbI controller. There is a chance the GFA synthesises a candidate GFbI controller that is unstable. For an unstable GFbI controller, assumption 1 does not hold and the pseudo-sensitivity is not valid. However, as the pseudo-sensitivity is computed anyway due to the lack of a stability check, there is a chance that this unstable candidate GFbI controller performs well based on frequency-domain performance metrics. This may lead to the GFA finding an unstable GFbI controller as the optimal solution in the design space. Therefore, the bounds on the optimisation parameters need to be chosen such that no unstable candidate GFbI controller can be designed with any combination of the optimisation parameters.

Suitable bounds can be found by iteratively changing the bounds until a seemingly optimal solution is found that is not on any of the bounds. A safe method is to assume the optimal solution to be in the vicinity of the initial point, which corresponds to the parameter values of the reference linear system. After running the GFA once with tight bounds around the initial point, the returned solution is inspected to see if the solution is equal to one or several of the bounds. If so, the solution is suboptimal. The bounds of parameters that are on the bound are changed and the GFA is run again. This process is repeated until the returned solution is no longer on any of the bounds.

Alternatively, the bounds can be initialised far away from the initial point such that the returned solution corresponds to an unstable GFbI controller, which can be tested experimentally or sometimes by inspection of the pseudo-sensitivity, where the pseudo-sensitivity shows unrealistically aggressive performance prediction. Subsequently, the bounds are tightened and the GFA is run again and the returned solution is tested for whether the GFbI controller is stable. If not, the bounds are tightened more and the process is repeated. This method has a chance of finding an improved global optimum compared to the former method.

4-4-3 Objective function costs

All cost sources contribute to a single objective function. A distinction is made between cost sources of type 1 that require a HOSIDF analysis of the candidate GFbI controller and cost sources of type 2 that additionally require computing the pseudo-sensitivity. The cost sources are the following:

Source type 1 | Requires HOSIDFs

Source 1.1: Open-loop constraints

Source type 2 | Requires pseudo-sensitivity

Source 2.1: Pseudo-sensitivity constraints

Source 2.2: Number of resets constraint

Source 2.3: Tracking constraint

Source 2.4: Optimisation target

The total cost follows as the sum of all cost sources, denoted as

$$c_{\text{tot}} = c_{1.1} + c_{2.1} + c_{2.2} + c_{2.3} + c_{2.4}, \tag{4-26}$$

where $c_{x.y}$ is the cost of source y of source type x. Some cost sources can have multiple costs associated with them. For example, there can be more than one open-loop constraint, in which case $c_{1.1}$ is simply the sum of the cost of each open-loop constraint.

As the HOSIDFs are needed to compute the pseudo-sensitivity, they are computed first. Subsequently, the cost of all type 1 cost sources is computed. If any constraint that is of a type 1 cost source is violated, the candidate GFbI controller is already known at this point not to be feasible. Hence, the computationally expensive pseudo-sensitivity does not need to be computed. The cost of all type 2 cost sources is not computed and assigned a cost of 10^9 instead. With all costs for this candidate GFbI controller known, the total cost is computed as in (4-26).

Recalling that the cost of a violated constraint using the violation metric is in the order of magnitude of 10^6, c_{tot} can only reach the order of magnitude of 10^9 if any constraint of a type 1 cost source is violated. This ensures the GFA does not have a local minimum where type 2 cost sources are being optimised while one or multiple type 1 constraints remain violated.

If no constraints of type 1 cost sources are violated, the pseudo-sensitivity is computed next, followed by the cost of all type 2 cost sources. Subsequently, the total cost is computed using (4-26).

4-4-4 Optimisation algorithms details

`Simulated annealing` runs differently from the other three global optimisation algorithms due to its nature. Firstly, the algorithm runs the hybrid function both at the end and at regular intervals. Running at intervals would not make sense for the other three algorithms due to their nature. Additionally, `simulated annealing` needs an initial point, which is chosen as the best solution from the other three algorithms, including their hybrid function. Implemented in this way, `simulated annealing` tries to further improve upon the best solution out of the three found by the other algorithms. `Simulated annealing` is the only global optimisation algorithm of the four used that cannot run in parallel, making it the least time-efficient algorithm. It is still included in the GFA for its entirely different approach to finding a global optimum than the other three global optimisation algorithms.

4-4-5 Optimisation algorithms options

The global optimisation algorithms are given options such that sufficient performance is obtained within a reasonable time frame. Sections 5-2-6 and 5-3-6 give an example of the time frame required to run the GFA for a use case with the options provided in this section. The options are based on the available options in the MATLAB commands for the respective algorithms. Options that are not stated in this section are left at their default. Options for the hybrid function are listed only under its respective header, even though it is run in conjunction with the global optimisation algorithms. Except for `simulated annealing`, all algorithms are run using parallel processing. Because of this, several options are based on the number of available cores #cores on the machine the GFA is run on. This is to maximise efficiency by reducing cases where many cores are waiting for one or a few cores to finish. Additionally, several options are related to the number of optimisation parameters #optparms to ensure the algorithm is robust to changes in optimisation parameters.

`Particle swarm/genetic algorithm` The function value tolerance is 0.001. The maximum number of stall iterations/generations is 30. To allow the algorithm to run until sufficient stall iterations/generations are achieved, the maximum number of iterations/generations is increased to infinity. The swarm/population size is $100 \cdot$ #optparms rounded up towards the nearest integer multiple of #cores.

`Surrogate optimisation` The maximum number of iterations is 10000. The minimum number of surrogate points is $\#\text{cores} \cdot$ #optparms.

`Simulated annealing` The function value tolerance is 0.001. The maximum number of stall iterations is $500 \cdot$ #optparms and the maximum number of iterations is $3000 \cdot$ #optparms. The maximum time the algorithm is allowed to run is 5 hours. The interval at which the hybrid function is run is 15 minutes.

`Pattern search` The function value tolerance and mesh size tolerance are 0.000001. To allow the algorithm to run until the function value or mesh size tolerance is achieved, the maximum number of iterations is increased to infinity. The algorithm is forced to complete all polls around the current point before continuing to the next iteration.

With these options, the global optimisation algorithms all run for a comparably long time.

For a candidate GFbI controller that satisfies all constraints, the only nonzero cost source is the

optimisation target. The unit of this cost source is absolute values. As such, the function value tolerance of the optimisation algorithms is also in absolute values.

Chapter 5

Validation

This chapter provides validation of the contributions presented in this work through two distinct use cases. The first is by assessing the performance of two optimised GFbI controllers, one with a serial and one with a parallel sequence, by having a simulated wire bonder track a reference signal. The performance is compared to that of a linear controller optimised by an autotuner. Subsequently, this is repeated with a physical wire bonder.

A control system or RCS with one of the two wire bonders that is controlled by any of the three controllers, namely the linear controller, the serial GFbI controller, or the parallel GFbI controller, is further referred to as the linear system, serial system, or parallel system, respectively.

Some numerical results cannot be provided due to confidentiality. For example, the exact controller parameters are not provided. The frequency for all plots containing frequency data on the X-axis has been divided by the sampling frequency.

First, Section 5-1 elaborates on the simulated and physical wire bonders and the wire bonding process. Subsequently, Section 5-2 presents the validation with the simulated wire bonder, followed by validation using the physical wire bonder in Section 5-3.

5-1 Wire bonders

This section elaborates on the use case for validation of the contributions this work provides. Firstly, Section 5-1-1 explains the wire bonding process, providing the background of how wire bonders operate. Subsequently, Sections 5-1-2 and 5-1-3 provide details on the hardware, constraints and linear control of the simulated and physical wire bonder, respectively. Note that the simulated wire bonder is not a simulation of the physical wire bonders, but of an entirely different wire bonder.

5-1-1 Wire bonding process

A wire bonder is a machine that places conducting wires between an integrated circuit and its packaging, forming a microchip. The machine bonds the two ends of the wire with their underlying surface by applying thermal or ultrasonic energy. Figure 5-1 illustrates a typical cycle of the wire bonding process utilising the “free air ball” technique [28].

Figure 5-2 shows the general shape of the reference signal used for the horizontal movement. The movement has been divided into three distinct stages. The first is the tracking stage, where the end-effector translates from one bonding surface to the other. The second stage is the set-

tling stage. This stage gives time for the end-effector's oscillations to settle within acceptable bounds for the third and final stage, the bonding stage. Drawn around the reference signal are permissible error bounds for the end-effector. These bounds are necessary to avoid contact with other wires that are already bonded and other surrounding objects during the tracking and settling stage. Additionally, the bounds during the bonding stage are necessary to remain on the bond pads. As such, the boundaries may at no point be exceeded during the wire bonding process.

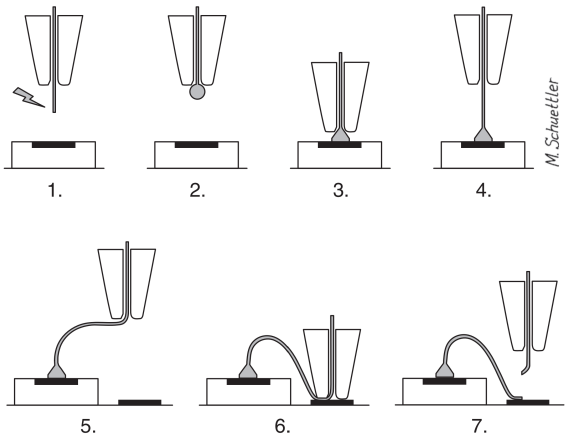

Figure 5-1: A cycle of the wire bonding process [28].

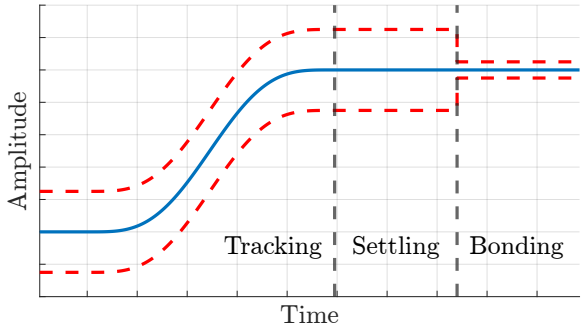

Figure 5-2: Typical reference signal during horizontal movement of the end-effector in a typical cycle of the wire bonding process, as illustrated in Figure 5-1.

5-1-2 Simulated wire bonder

This section details the hardware of the simulated wire bonder, the constraints imposed on the control system, and the linear controller for this plant that is used as a reference for validating the contributions of this work.

Hardware

The simulated wire bonder is modelled using Simscape Multibody, a 3D CAD tool developed by MATLAB. The motion platform of the simulated wire bonder has three degrees of freedom (DOF), which are controlled using a Cartesian coordinate system. This is illustrated in Figure 5-3. The figure also shows the base frame, which mainly functions as vibration isolation between the stages and the external world. For each axis, there is a separate actuator directly applying a force to the stage. For this work, the focus is on the X-stage. Additionally, for this work, all three stages are assumed to be completely uncoupled from each other. This allows for modelling the X-stage as a SISO system, with force applied on the X-axis as input and X-axis displacement as output.

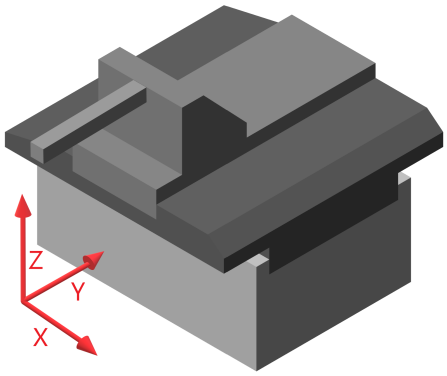

Figure 5-3: Simplified Simscape Multibody model of the simulated wire bonder motion platform.

Figure 5-4 shows the FRF of the simulated wire bonder mapping from the force on the X-stage to the X-stage displacement. The FRF is of the linearised system measured around the system configuration with all three stages at their centre position. The system has a transport delay, which originates from a delay between sensor readings

and system actuation. Additionally, two resonances are visible in the FRF. There are modes present in the system that affect the X-stage that are hardly observable from the plant's FRF the low-frequency region, as will be shown in the simulation results in Section 5-2.

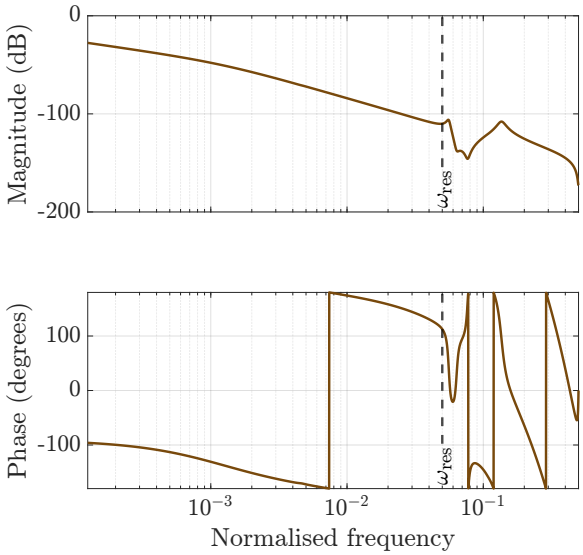

Figure 5-4: FRF of the simulated wire bonder. The FRF maps from the force on the X-axis to the displacement of the X-axis.

Constraints

Two constraints are imposed on the control system of the simulated wire bonder. Firstly, the maximum error amplification is limited by imposing a constraint on the maximum sensitivity using (2-4) with $S_{\text{lim}} = 6$ dB. Secondly, to limit the sensitivity after ω_{res}, a constraint in imposed on the maximum open-loop gain using (2-7) with $L_{\text{lim}|\omega \geq \omega_{\text{res}}} = -12$ dB.

Linear control

The simulated wire bonder is controlled using an automatically tuned linear controller. Figure 5-5 shows a Bode plot of the linear controller. The controller is designed based solely on an FRF of the plant and is tuned such that it meets the constraints. Figure 3-1 shows a schematic representation of the linear controller with transfer functions (3-1) to (3-3). The controller element C_{notches} contains two skewed notch filters. As the normal operating condition of this wire bonder is with feedforward control enabled in a control loop as shown in Figure 2-1, an automatically tuned feedforward controller is employed for validation in this work using this wire bonder. Both the linear feedback and feedforward controller are designed by the company providing the simulated wire bonder.

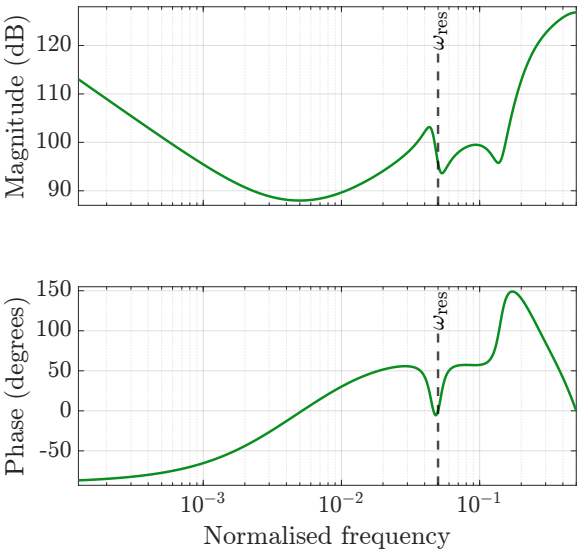

Figure 5-5: Bode plot of the linear controller for the simulated wire bonder.

Figure 5-6 shows the sensitivity of the linear control system. The waterbed effect limits reference tracking performance from increasing without also further amplifying the noise or increasing the range of amplified frequencies. Although it is certainly possible to further tune this linear controller slightly better for improved reference tracking while remaining within the constraints, the waterbed effect inherently limits this improvement of the LTI controller at some point. Therefore, NLTI control techniques such as reset control are necessary to further improve reference tracking.

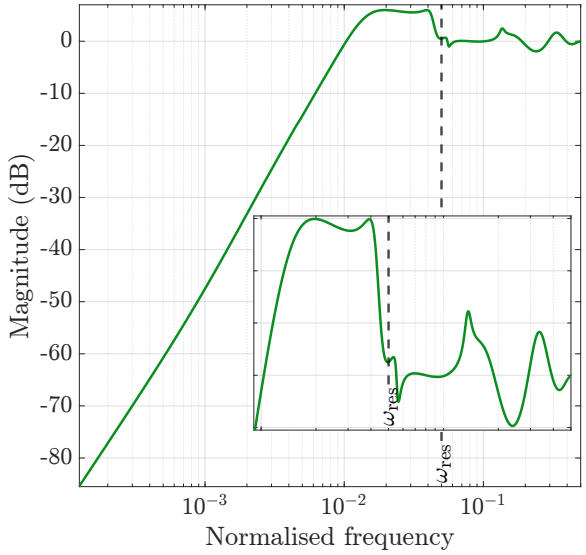

Figure 5-6: Sensitivity of the simulated wire bonder with the linear controller.

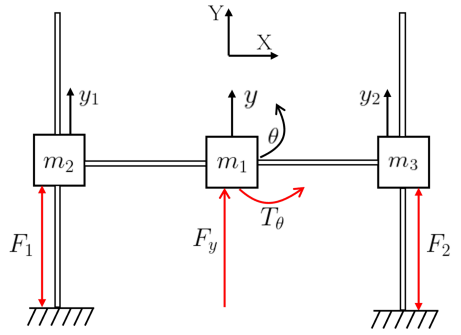

Figure 5-7: Schematic representation of the physical wire bonder motion platform [29].

5-1-3 Physical wire bonder

This section details the hardware of the physical wire bonder, the constraints imposed on the control system, and the linear controller for this plant that is used as a reference for validating the contributions of this work.

Hardware

The motion platform of the physical wire bonder has three DoF. These are controlled using three generalised coordinates, namely vertical translation along the Z-axis, horizontal translation y along the Y-axis and rotation θ about the Z-axis. This is illustrated in Figure 5-7. Three actuators apply a force on the Z-axis (not shown in the figure) and on the two outer masses. This is transformed to the generalised forces and torque F_z (not shown in the figure), F_y, and T_θ. This work focuses on the control of displacement y by controlling the generalised force F_y. The generalised coordinates are assumed to be completely uncoupled from each other regarding the control thereof.

Figure 5-8 shows the FRF of the physical wire bonder mapping from generalised force F_y to displacement y. The FRF is of the linearised system measured around the system configuration with all three actuators at their centre position. The system has a transport delay, which originates from a delay between sensor readings and system actuation.

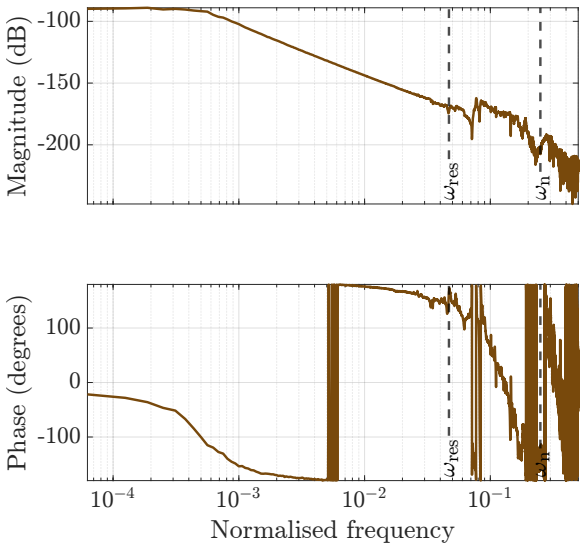

Figure 5-8: FRF of the physical wire bonder. The FRF maps from generalised force F_y to displacement y.

Constraints

Three constraints are imposed on the control system of the physical wire bonder. Firstly, the

maximum error amplification is limited by imposing a constraint on the maximum sensitivity using (2-4) with $S_{\text{lim}} = 6$ dB. Secondly, to limit the sensitivity after ω_{res}, a constraint in imposed on the maximum open-loop gain using (2-7) with $L_{\text{lim}|\omega \geq \omega_{\text{res}}} = -12$ dB. Thirdly, to prevent the controller from drawing too much current in response to measurement noise, a constraint is indirectly imposed on the maximum control sensitivity using (2-13) with $L_{\text{lim}|\omega \geq \omega_{\text{high}}} = -25$ dB and $\omega_{\text{high}} = \omega_{\text{n}}$.

Linear control

The physical wire bonder is controlled using an automatically tuned linear controller. Figure 5-9 shows a Bode plot of the linear controller. The controller is designed based solely on an FRF of the plant and is tuned such that it meets the constraints. Figure 3-1 shows a schematic representation of the linear controller with transfer functions (3-1) to (3-3). The controller element C_{notches} contains two skewed notch filters. Note that the linear controller of the simulated and physical wire bonder have the same controller elements, but the controller elements have different parameters. As the normal operating condition of this wire bonder is with feedforward control enabled in a control loop as shown in Figure 2-1, an automatically tuned feedforward controller is employed for validation in this work using this wire bonder. Both the linear feedback and feedforward controller are designed by the company providing the physical wire bonder.

Figure 5-10 shows the sensitivity of the linear control system. The waterbed effect limits reference tracking performance from increasing without also further amplifying the noise or increasing the range of amplified frequencies. Although it is certainly possible to further tune this linear controller slightly better for improved reference tracking while remaining within the constraints, the waterbed effect inherently limits this improvement of the LTI controller at some point. Therefore, NLTI control techniques such as reset control are necessary to further improve reference tracking.

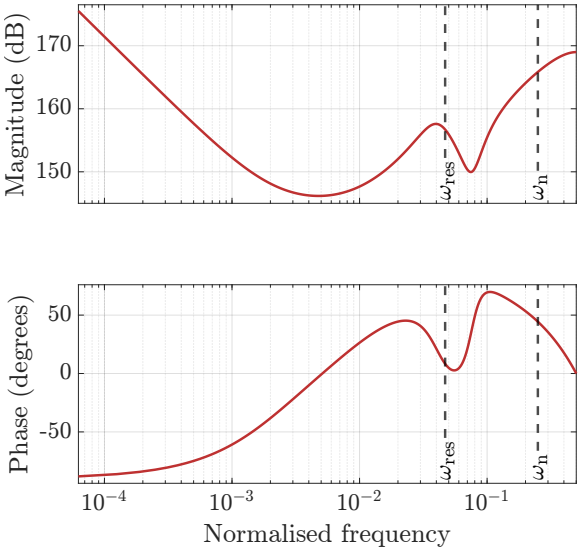

Figure 5-9: Bode plot of the linear controller for the physical wire bonder.

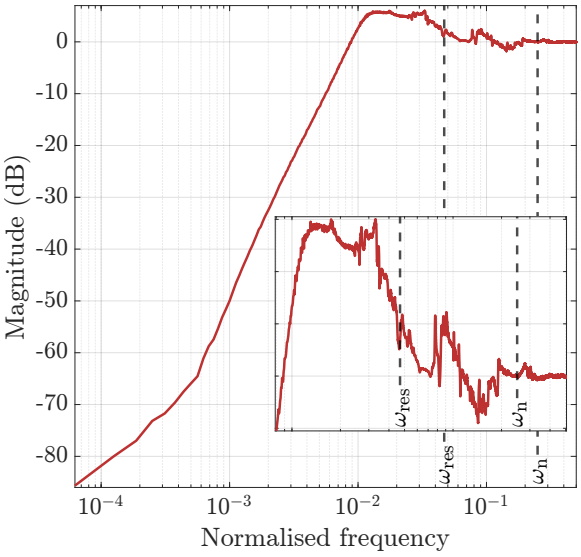

Figure 5-10: Sensitivity of the physical wire bonder with the linear controller.

5-2 Simulation results

This section presents the validation using the simulated wire bonder. "The control system" and "the RCS" refers to the simulated wire bonder with one of the three controllers intended for this plant

for the remainder of this section. The value of ω_{res} is redacted, but it is shown in the figures further on in this section.

First, Section 5-2-1 presents the conditions under which the GFA is run for the simulation RCS. Subsequently, Section 5-2-2 presents the optimised controllers, followed by an analysis of the open loop, the closed loop, and the time-domain results in Sections 5-2-3 to 5-2-5, respectively. Finally, Section 5-2-6 presents an overall analysis of the results and reflects upon the contributions of this work in light of the validation results of the simulated wire bonder.

5-2-1 Optimisation conditions

Some parameter values used during validation using the simulation RCS are redacted and hence only provided relatively or not at all. Redacted parameters that are required for qualitative validation are illustrated in the associated figures further in the chapter. Parameters that can be provided numerically are presented in Table 5-1.

The number of resets constraint and tracking constraint are active. Additionally, the GFA imposes one open-loop constraint and one pseudo-sensitivity constraint on the simulation RCS, namely replicating the constraints imposed on the linear control system. The open-loop constraint is imposed on the first harmonic of the open-loop, namely the SIDF. This is under the assumption that the sensitivity of all HOSIDFs are significantly lower than the pseudo-sensitivity compared to the SIDF and consequently contribute significantly less to the pseudo-sensitivity.

Upon making a forward or backward move with the X-stage, a distinct dominant low-frequency vibration is observed in the error signal that originates from the base frame of the wire bonder. This base frame vibration is illustrated in Figure 5-11. Even though the base frame vibration is not limiting the performance of the simulated wire bonder with the linear controller such that the error signal would be out of the specifications, it poses a clear-cut opportunity to validate whether the GFA can design a nonlinear controller to improve upon this linear controller by suppressing the base frame vibration. Therefore, the optimisation target contains one frequency region, illustrated in Section 5-2-4, that targets the base frame vibration.

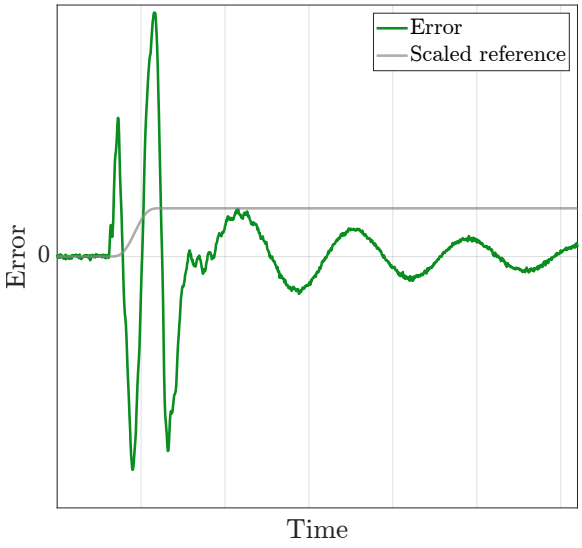

Figure 5-11: Error signal of the linear system tracking the shown reference signal. The base frame vibration can clearly be observed on the right.

All figures that contain data of an RCS and have the frequency on the X-axis start at ω_{skip}, with the exception of close-ups. The true value of ω_{skip} is redacted.

Of all the controller element parameters of the GFbI controllers available for optimisation, the GFA has optimised the proportional gain, integrator frequency, lead filter frequency, and γ. Note that ω_{c} is optimised internally. These parameters pertain mostly to the low- and middle-frequency behaviour of the control system, which is where the GFA was instructed to improve performance by means of the targeted frequency regions as will be shown further on in the chapter. Moreover, adding the notch filters and lag filter often resulted in the GFA finding unstable GFbI controllers, such that the bounds would need to be rather tight. Additionally, adding more parameters increases the runtime of the GFA, making it infeasible in terms of time.

Table 5-1: Parameters used to run the GFA for the simulated wire bonder. Some parameters are redacted and consequently are not included in the table.

Parameter	Value	Reference
S_{skip}	-40 dB	(4-6)
f_{exp}	2	(4-9)
n_{exp}	5	(4-9)
$L_{\text{lim,con}}$	-12 dB	(4-12)
$\omega_{L_{\text{low}}}$	ω_{res}	(4-13)
$\omega_{L_{\text{high}}}$	ω_{N}	(4-13)
$S_{\text{lim,con}}$	6 dB	(4-15)
$\omega_{S_{\text{low}}}$	ω_{skip}	(4-16)
$\omega_{S_{\text{high}}}$	ω_{N}	(4-16)

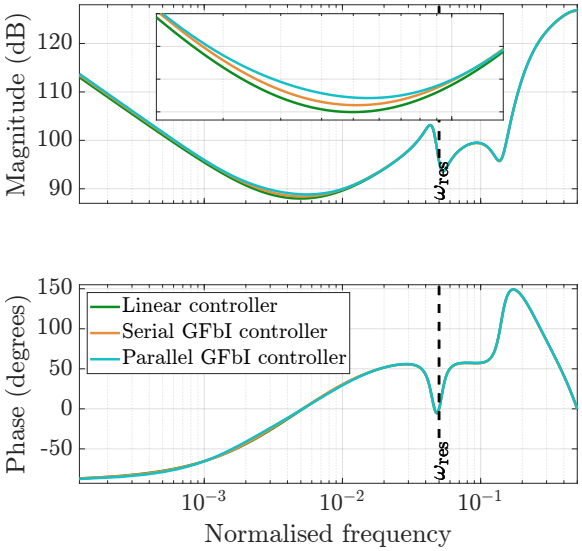

Figure 5-12: Magnitude and phase characteristics of the controllers for the simulated wire bonder.

5-2-2 Optimised controllers

Figure 5-12 shows the linear controller and SIDF of the two GFbI controllers. In the low-frequency region, the magnitudes of the three controllers are within a range of 0.8 dB difference from each other. The parallel GFbI controller has the largest magnitude, followed by the serial GFbI controller, and the linear controller has the smallest magnitude. The difference is the largest in the middle-frequency region, shown in the close-up, where the largest difference is around 1 dB.

5-2-3 Open loop analysis

Figure 5-14 shows the magnitude characteristics of the SIDF and the first 25 HOSIDFs of the open-loop serial and parallel system. The figure shows that the HOSIDFs of the parallel system, compared to the serial system, have a higher magnitude in the low-frequency region and a lower magnitude in the middle- and high-frequency region. For both RCSs, the HOSIDFs are increasingly close together for increasing order. Additionally, the magnitude difference between the SIDF and the HOSIDFs is significantly larger than the magnitude difference among the HOSIDFs.

Figure 5-13 shows the magnitude and phase characteristics of the open-loop control systems. Both the serial and parallel system has a higher bandwidth than the linear system. The serial and parallel system have a higher and lower phase margin than the linear controller, respectively. Both RCSs satisfy the open-loop constraint.

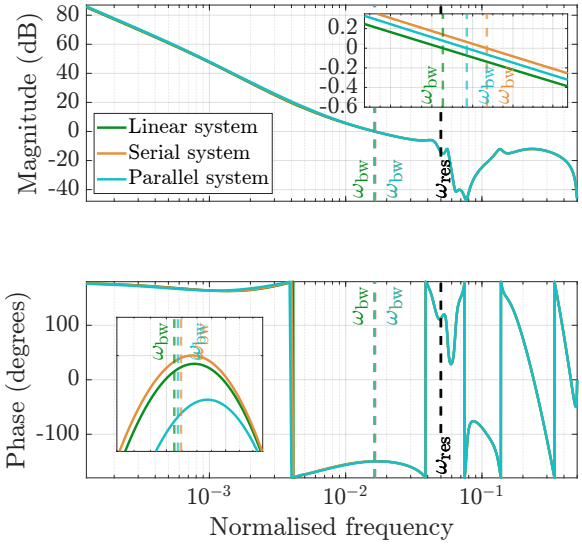

Figure 5-13: Magnitude and phase characteristics of the open-loop control systems.

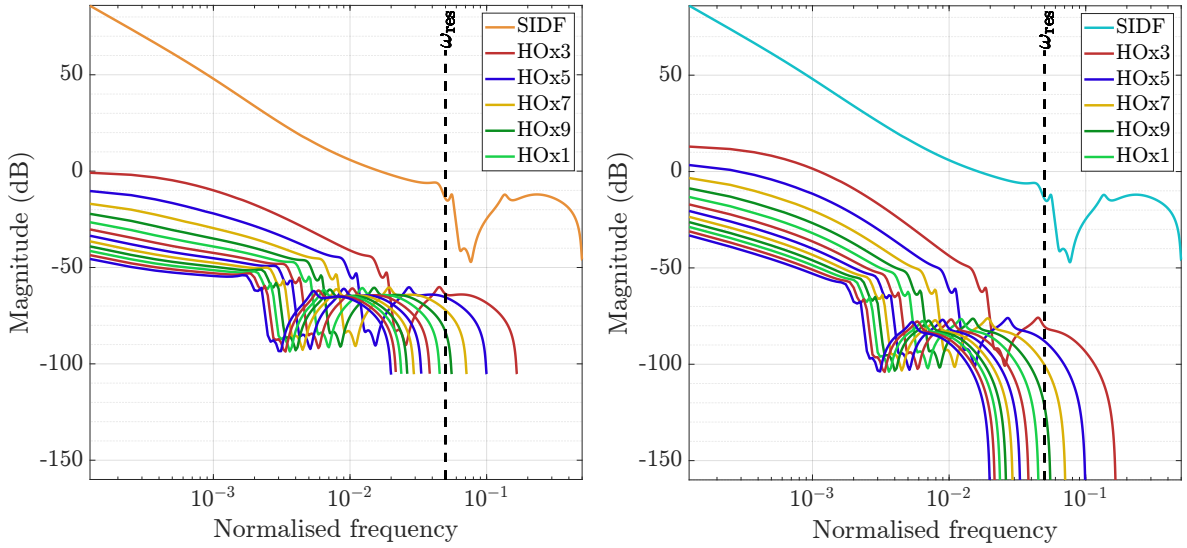

(a) Serial system. **(b)** Parallel system.

Figure 5-14: Magnitude characteristics of the SIDF and the first 25 HOSIDFs of the open-loop serial and parallel system. The highest HOSIDF is of the lowest order, where the order increases for each consecutive lower HOSIDF.

5-2-4 Closed loop analysis

Figure 5-16 shows the pseudo-sensitivity and sensitivity of the first 25 HOSIDFs of the closed-loop serial and parallel system. The sensitivity of the HOSIDFs of the parallel system, compared to the serial system, has a higher magnitude in the low-frequency region and a lower magnitude in the middle- and high-frequency region. This corresponds to what is observed in the open loop. For both RCSs, the sensitivity of the HOSIDFs is increasingly close together for increasing order. Additionally, the magnitude difference between the SIDF and the HOSIDFs is significantly larger than the magnitude difference among the HOSIDFs. Thus, the pseudo-sensitivity is similar to the sensitivity of the SIDF and the HOSIDFs have a minor, although nonzero, impact.

Figure 5-15 shows the sensitivity and pseudo-sensitivity of the closed-loop control systems. The frequencies between the two dotted lines in Figure 5-15 is the targeted frequency region. Both RCSs satisfy the pseudo-sensitivity constraint.

Figure 5-17 shows a close-up of the frequency region where the tracking constraint is active. The figure shows that both the serial and parallel system satisfy the tracking constraint. The figure also shows that the parallel system has a lower pseudo-sensitivity than the serial system for almost the full frequency region of the tracking constraint.

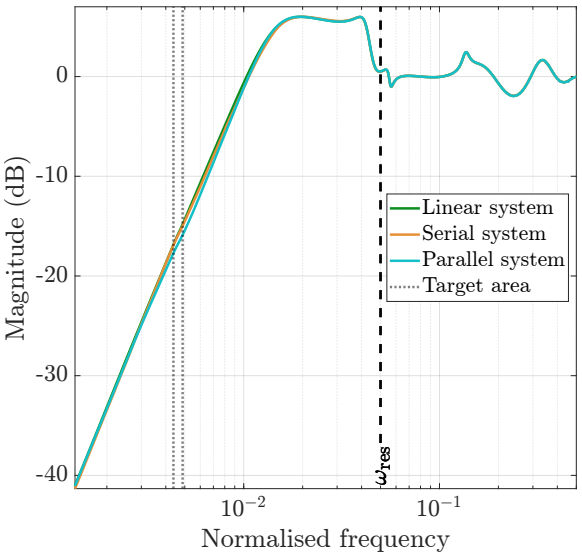

Figure 5-15: Sensitivity and pseudo-sensitivity of the closed-loop control systems.

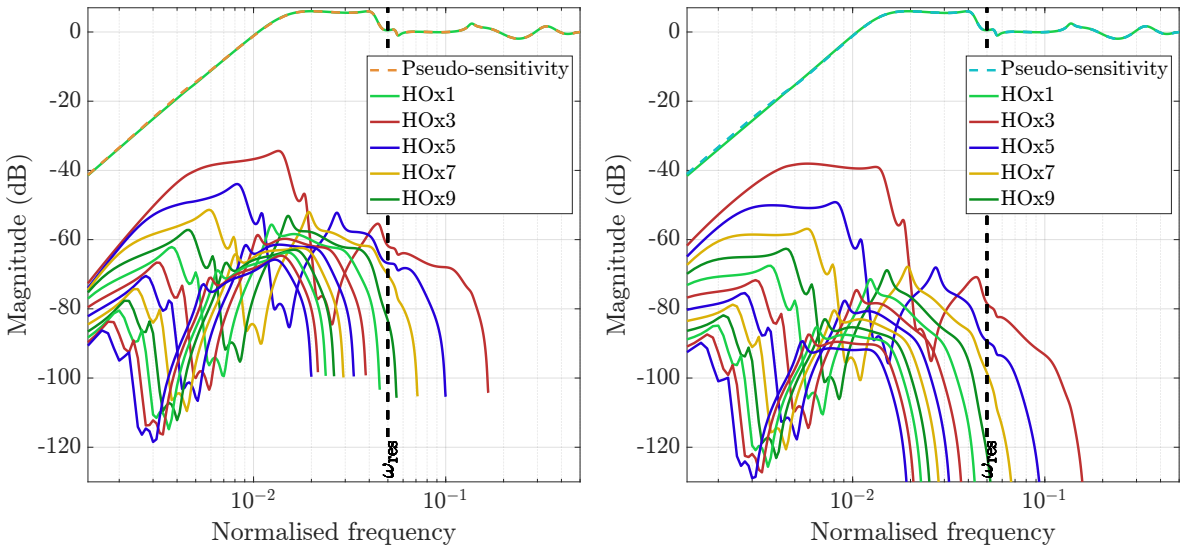

(a) Serial system. **(b)** Parallel system.

Figure 5-16: Pseudo-sensitivity and sensitivity of the first 25 HOSIDFs of the closed-loop control systems. The highest HOSIDF is of the lowest order, where the order increases for each consecutive lower HOSIDF.

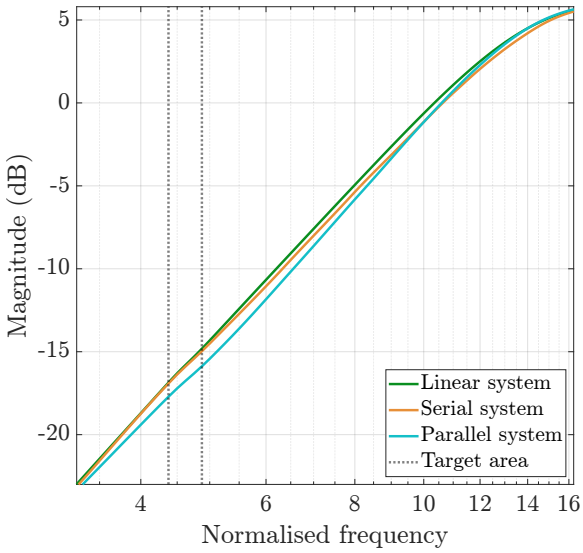

Figure 5-17: Sensitivity and pseudo-sensitivity of the closed-loop control system at the frequency region where the tracking constraint is active.

Figure 5-18 shows a close-up of the targeted frequency region. Both the serial and parallel system has a pseudo-sensitivity lower than the linear system's sensitivity across the full targeted frequency region. The parallel system achieves this better than the serial system.

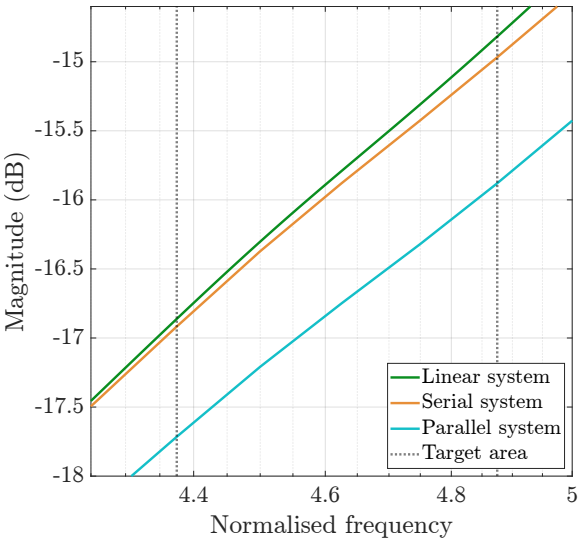

Figure 5-18: Targeted frequency region of the sensitivity and pseudo-sensitivity of the closed-loop control systems.

5-2-5 Time domain analysis

The developed GFbI controllers for the simulated wire bonder are tested by simulating the wire bonder to track the reference signal shown in Figure 5-19 with white noise added to the output signal to simulate measurement noise of the encoders. The signal consists of one smooth step-up and step-down. After each step, a settling region is defined that starts from the moment the reference signal becomes stationary and runs until the start of the next step or until the end of the reference signal. The bounds denoted by black dashed lines in the following figures of the error signal indicate instant settling, i.e. if the error signal instantly settles to within the specifications. This is equivalent to a settling region in Figure 5-1 of zero length.

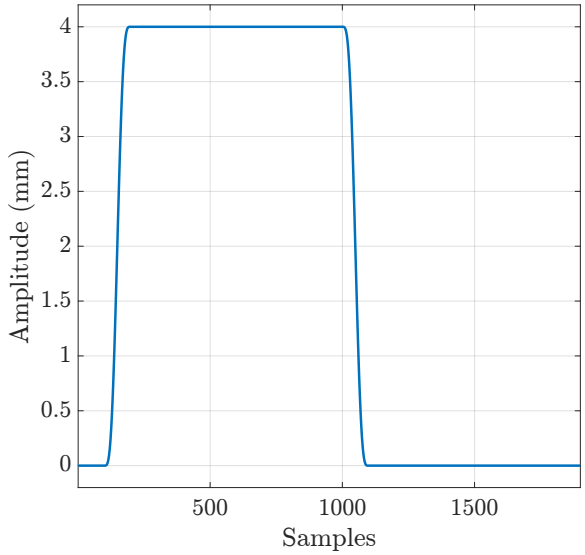

Figure 5-19: Reference signal for validation using the simulated wire bonder.

Figure 5-20 shows the error signal for the settling region after the step-up. The base frame vibration is clearly observable. The parallel system settles first, followed by the serial system and lastly the linear system. The effect of the state resets is visible in the error signal of both the serial and parallel system. The parallel system generally suppresses the base frame vibration the best in this settling region, as follows from the reduced amplitude at the peaks of the base frame vibration.

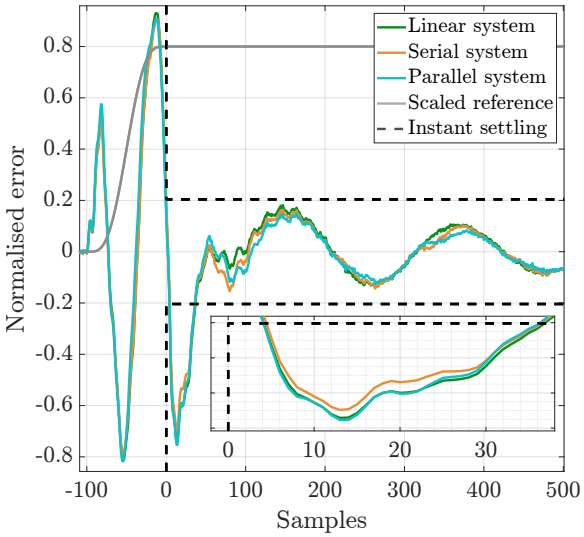

Figure 5-20: Error signal during tracking of the step-up in the reference signal by the control systems.

Figure 5-20 shows the error signal for the settling region after the step-down. The same observations are made as for the step-up.

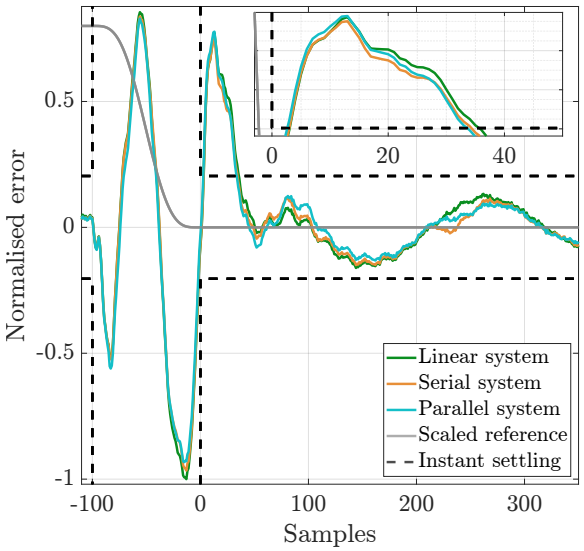

Figure 5-21: Error signal during tracking of the step-down in the reference signal by the control systems.

Figure 5-22 shows the power spectral density (PSD) of the error in the settling region after the

step-up. The base frame vibration is clearly observable as a peak at low frequency. As shown, the GFbI controllers reduce this peak compared to the linear controller, as is also observed in the error signal. Additionally, higher-order harmonics of the base frame vibration as a result of the state resets are visible in the PSD as extra peaks to the right of the base frame vibration that are not present in the linear system's PSD. As expected from the diminishing magnitude of the HOSIDFs' sensitivity, the power of each consecutive higher-order harmonic is diminished compared to the previous. The targeted frequency range the GFA used for the tuning of the GFbI controllers is a small range around the frequency of the base frame vibration identified from the PSD.

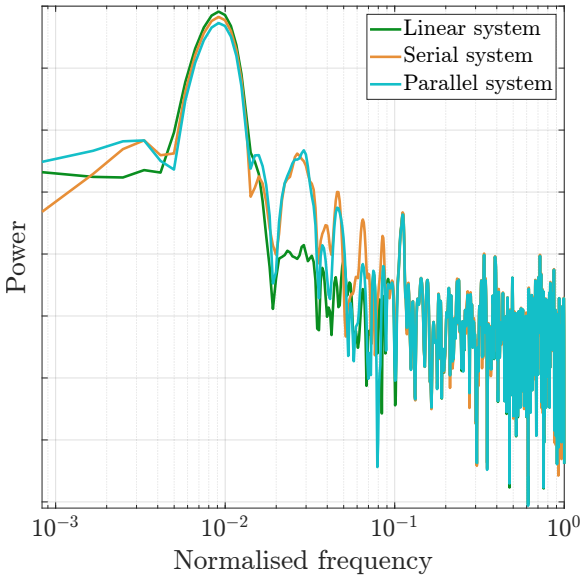

Figure 5-22: Power spectral density of the error in the settling region after the step-up padded with zeros two times the length of the error signal and convolved with a Hann window.

Figure 5-23 shows the cumulative PSD (CPSD) of the error in both settling regions. The power has been normalised such that the maximum power of the linear system's CPSD equals 1. The figure shows the linear, serial and parallel system to have the most power in the error signal in the stated order. The base frame vibration contributes the most to the cumulative power, where the serial and parallel system also show a additional small increase in cumulative power at the frequency of the higher-order harmonics.

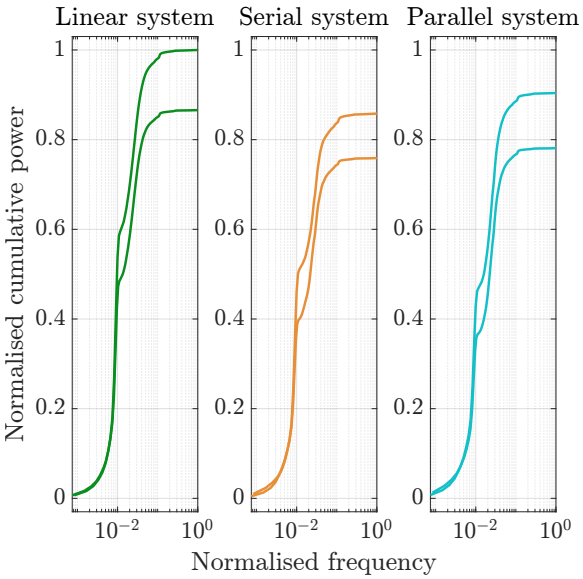

Figure 5-23: Cumulative power spectral density of the error in both settling regions padded with zeros two times the length of the error signal and convolved with a rectangular window.

Table 5-2 presents the settling time, measured in samples, for both settling regions. The settling time is defined as the time between the start of the settling region until the error signal crosses the bound for the last time during the settling region. The settling time is interpolated between the last sample outside and inside of the bound. The indicated settling time changes are with respect to the linear system.

Table 5-3 presents the root-mean-square error (RMSE) of the error signals between the moment each signal settles until the end of the settling regions. The base frame vibration is dominant mostly in the aforementioned region of the error signal, and not prior to settling. Therefore, the error signal prior to settling is not considered in the RMSE, in line with the purpose of showing the GFA tunes the GFbI controllers to suppress the base frame vibration. The RMSE is computed using the normalised error shown in Figures 5-20 and 5-21.

Table 5-2: Settling time after each step in the reference signal.

Settling region	Settling time linear system (samples)	Settling time serial system (samples)	Settling time parallel system (samples)	Change serial system (%)	Change parallel system (%)
step-up	36.778	36.414	36.213	-0.989	-1.538
step-down	35.625	34.306	33.557	-3.701	-5.805

Table 5-3: RMSE for each settling region.

Settling region	RMSE linear system (normalised)	RMSE serial system (normalised)	RMSE parallel system (normalised)	Change serial system (%)	Change parallel system (%)
step-up	0.0731	0.0685	0.0610	-6.335	-16.473
step-down	0.0627	0.0564	0.0526	-9.991	-16.016

The indicated RMSE changes are with respect to the linear system.

Table 5-4 presents statistics based on the settling time and RMSE of both settling regions. Both the serial and parallel system outperform the linear system in terms of median settling time and RMSE. Additionally, the parallel system outperforms the serial system, especially in the RMSE where it shows a decrease of twice as much as the serial system.

Table 5-4: Statistics based on the settling time and RMSE of Tables 5-2 and 5-3.

Metric	Serial system	Parallel system
Best settling time change (%)	-3.701	-5.805
Worst settling time change (%)	-0.989	-1.538
Median settling time change (%)	-2.345	-3.671
Median RMSE change (%)	-8.163	-16.245

5-2-6 Overall analysis

The GFbI controllers were optimised on a virtual machine with a "Common KVM processor" with 16 virtual processors and 64 GB of RAM. The runtime of the GFA to optimise GFbI controllers for the simulated wire bonder was roughly 9 hours per controller. The solution for the serial GFbI controller was found by `genetic algorithm` combined with `simulated annealing`. The solution for the parallel GFbI controller was found by `particle swarm`. Table 5-5 presents further information on the found solution and optimisation procedure, where "fevals" is the number of evaluations of the objective function of only the global optimisation algorithm that found the best solution, including function calls made by `pattern search` as part of that global optimisation. Numerical values for other controller element parameters are redacted.

Table 5-5: Data of the optimisation procedure and found solution of the GFbI controllers.

	Serial	Parallel
Final cost (dB)	-0.0553	-0.854
fevals	17878	26927
γ	0.769	0.400
ω_c/ω_i	0.694	0.452

The serial and parallel system both satisfy all the constraints. Therefore, as the number of resets constraint is satisfied, assumption 2 holds. Input-to-state convergence of the RCSs, relating to assumption 1, has not been proven mathemat-

ically. However, the time-domain results RCSs indicate the RCSs converges towards a steady-state response. This suggests assumption 1 also holds. The HOSIDF analysis of the open loop show the HOSIDFs to be considerably lower than the SIDF in open loop, indicating that resets are mainly triggered by the SIDF. Therefore, it is assumed that assumption 3 reasonably holds.

In Section 5-2-1 the assumption was made that the pseudo-sensitivity is close to the sensitivity of the SIDF in the RCSs. The HOSIDF analysis of the closed loop shows this to be generally true, indicating this assumption holds.

The optimisation target of the GFA is leveraged to suppress the base frame vibration. Frequency-domain performance prediction suggests the GFbI controllers both should do so better than the linear system, with the parallel GFbI controller showing the most promising prediction, as the pseudo-sensitivity near the frequency of the base frame vibration as identified using the PSD has the lowest magnitude. The time-domain results confirm the performance prediction, where indeed the base frame vibration is suppressed by both GFbI controllers while the settling time did not increase, but rather even decreased. The error signal shows a clear reduction in the amplitude of the error in the observed large sinusoid, where the state resets are clearly visible at the zero crossings. Moreover, the median RMSE of the serial and parallel system show a significant decrease. Additionally, the PSD shows a reduction in the power of the error signal at the base frame vibration frequency. In all metrics, the parallel system outperforms the serial system.

The intended effect of the parallel sequence compared to the serial sequence is to reduce the magnitude of the HOSIDFs by avoiding the generated higher-order harmonics, generated by the reset element, from passing through the lead filter in open loop. The HOSIDF analysis of the closed-loop RCSs shows the magnitude of the HOSIDFs of the serial and parallel system indeed changed, where the magnitude decreased at the middle- and high-frequency region, but increased at the low-frequency region. It cannot be concluded whether this is always the effect of changing the sequence in the specified manner, as the two GFbI controllers were tuned differently by the GFA. Thus, not only the sequence changed, but also the rest of the GFbI controller. To isolate the effect of changing the sequence, the rest of the GFbI controller must remain constant. What can be concluded, however, is that the parallel sequence allows the GFbI controller to better tune reducing the pseudo-sensitivity at the targeted frequency region, at least for these specific frequency regions.

5-3 Experimental results

This section presents the validation using the physical wire bonder. The results are similar to the validation with the simulated wire bonder. For completeness' sake, the interesting features in the results of the validation with the physical wire bonder are still pointed out in this section. "The control system" and "the RCS" refers to the physical wire bonder with one of the three controllers intended for this plant for the remainder of this section. The value of ω_{res} is redacted, but it is shown in the figures further on in this section.

First, Section 5-3-1 presents the conditions under which the GFA is run for the physical RCS. Subsequently, Section 5-3-2 presents the optimised controllers, followed by an analysis of the open loop, the closed loop, and the time-domain results in Sections 5-3-3 to 5-3-5, respectively. Finally, Section 5-3-6 presents an overall analysis of the results and reflects upon the contributions of this work in light of the validation results of the physical wire bonder.

5-3-1 Optimisation conditions

Some parameter values used during validation using the physical RCS are redacted and hence only provided relatively or not at all. Redacted parameters that are required for qualitative validation are illustrated in the associated figures further in the chapter. Parameters that can be provided numerically are presented in Table 5-6.

The number of resets constraint and tracking constraint are active. Additionally, the GFA imposes two open-loop constraints and one pseudo-sensitivity constraint on the physical RCS, namely replicating the constraints imposed on the linear control system. The open-loop constraints are

imposed on the first harmonic of the open-loop, namely the SIDF. This is under the assumption that the sensitivity of all HOSIDFs are significantly lower than the pseudo-sensitivity compared to the SIDF and consequently contribute significantly less to the pseudo-sensitivity.

The optimisation target is chosen such that the GFA tunes the GFbI controllers for a decreased settling time. Figure 5-24 shows the error signal of the linear system tracking the shown reference signal. Near the end of the transient response, roughly half a period of a sinusoid can be observed. The frequency of this sinusoid was estimated by hand, of which it should be noted is rather inaccurate given how fast the sinusoid decays. This estimation resulted in two frequency ranges in the middle-frequency region, which became the targeted frequency ranges for the GFA used for tuning of the GFbI controllers. The optimisation target are illustrated in Section 5-3-4.

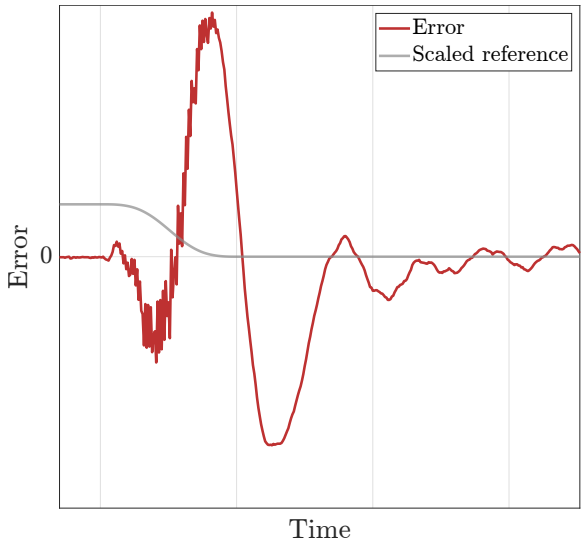

Figure 5-24: Error signal of the linear system tracking the shown reference signal. A dominant vibration right after the movement can be observed.

All figures that contain data of an RCS and have the frequency on the X-axis start at ω_{skip}, with the exception of close-ups. The true value of ω_{skip} is redacted.

The same controller element parameters for these GFbI controllers have been optimised by the GFA as for the GFbI controllers for the simulated wire bonder. These are the proportional gain, integrator frequency, lead filter frequency, and γ. Note that ω_c is optimised internally.

Table 5-6: Parameters used to run the GFA for the physical wire bonder. Some parameters are redacted and consequently are not included in the table.

Parameter	Value	Reference
S_{skip}	-40 dB	(4-6)
f_{exp}	2	(4-9)
n_{exp}	5	(4-9)
$L_{\text{lim},1,\text{con}}$	-12 dB	(4-12)
$\omega_{L_{\text{low},1}}$	ω_{res}	(4-13)
$\omega_{L_{\text{high},1}}$	ω_{N}	(4-13)
$L_{\text{lim},2,\text{con}}$	-25 dB	(4-12)
$\omega_{L_{\text{low},2}}$	ω_{n}	(4-13)
$\omega_{L_{\text{high},2}}$	ω_{N}	(4-13)
$S_{\text{lim,con}}$	6 dB	(4-15)
$\omega_{S_{\text{low}}}$	ω_{skip}	(4-16)
$\omega_{S_{\text{high}}}$	ω_{N}	(4-16)

5-3-2 Optimised controllers

Figure 5-26 shows the linear controller and SIDF of the two GFbI controllers. In the low-frequency region, the magnitudes of the three controllers are within a range of 0.7 dB difference from each other. The parallel GFbI controller has the largest magnitude, followed by the serial GFbI controller, and the linear controller has the smallest magnitude. The difference is the largest in the middle-frequency region, shown in the close-up, where the largest difference is around 0.9 dB.

5-3-3 Open loop analysis

Figure 5-25 shows the magnitude characteristics of the SIDF and the first 25 HOSIDFs of the open-loop serial and parallel system. The figure shows that the HOSIDFs of the parallel system, compared to the serial system, have a higher magnitude in the low-frequency region and a lower magnitude in the middle- and high-frequency region. For both RCSs, the HOSIDFs are increasingly close together for increasing order. Additionally, the magnitude difference between the SIDF and the HOSIDFs is

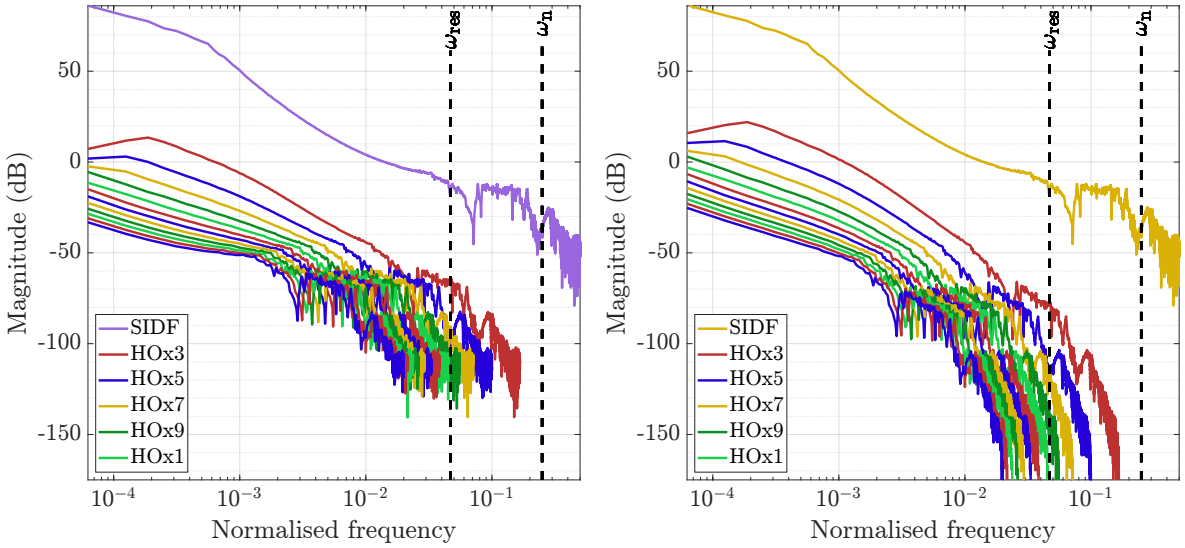

(a) Serial system. **(b)** Parallel system.

Figure 5-25: Magnitude characteristics of the SIDF and the first 25 HOSIDFs of the open-loop serial and parallel system. The highest HOSIDF is of the lowest order, where the order increases for each consecutive lower HOSIDF.

significantly larger than the magnitude difference among the HOSIDFs.

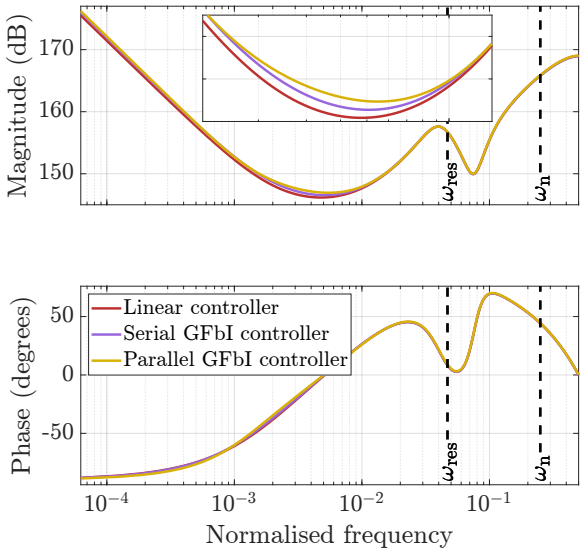

Figure 5-26: Magnitude and phase characteristics of the controllers for the physical wire bonder.

Figure 5-28 shows the magnitude and phase characteristics of the open-loop control systems. Both the serial and parallel system have a higher bandwidth than the linear system. The bandwidth of the serial and parallel system is nearly identical. The serial and parallel system also has a higher and lower phase margin than the linear controller, respectively. Both RCSs satisfy both open-loop constraints.

5-3-4 Closed loop analysis

Figure 5-27 shows the pseudo-sensitivity and sensitivity of the first 25 HOSIDFs of the closed-loop serial and parallel system. The sensitivity of the HOSIDFs of the parallel system, compared to the serial system, has a higher magnitude in the low-frequency region and a lower magnitude in the middle- and high-frequency region. This corresponds to what is observed in the open loop. For both RCSs, the sensitivity of the HOSIDFs is increasingly close together for increasing order. Additionally, the magnitude difference between the SIDF and the HOSIDFs is significantly larger than the magnitude difference among the HOSIDFs. Thus, the pseudo-sensitivity is similar to the sensitivity of the SIDF and the HOSIDFs have a minor,

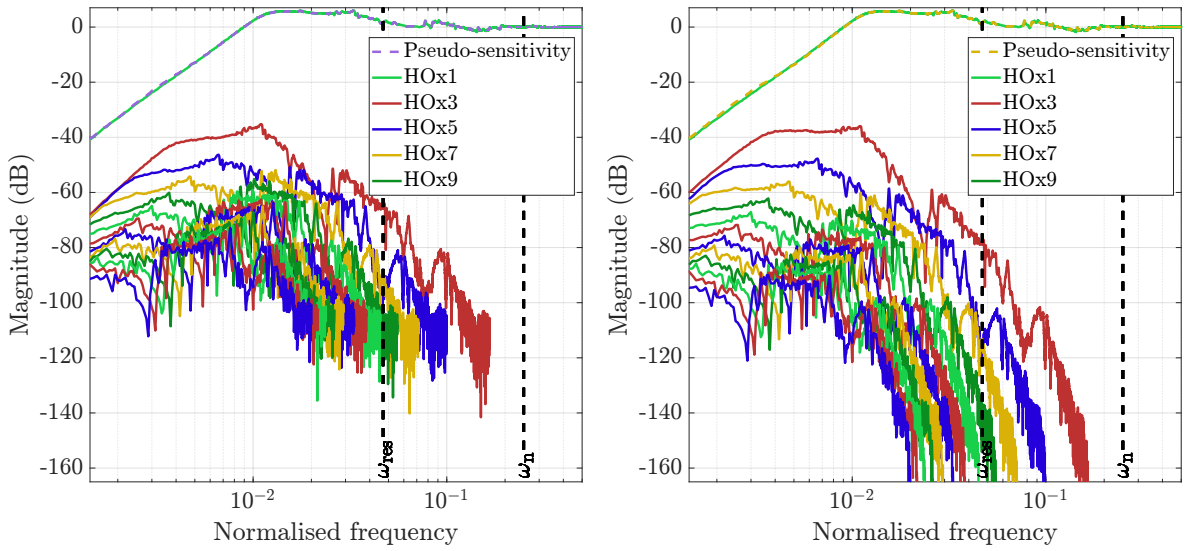

(a) Serial system. **(b)** Parallel system.

Figure 5-27: Pseudo-sensitivity and sensitivity of the first 25 HOSIDFs of the closed-loop control systems. The highest HOSIDF is of the lowest order, where the order increases for each consecutive lower HOSIDF.

although nonzero, impact.

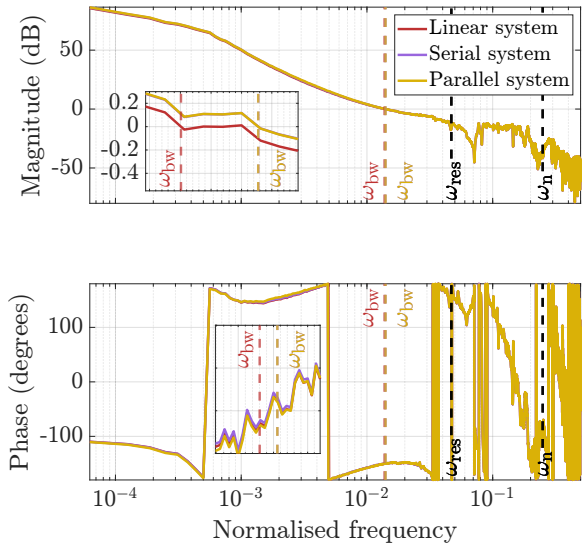

Figure 5-28: Magnitude and phase characteristics of the open-loop control systems. The dashed line indicating the bandwidth of the serial system is hidden under that of the parallel system.

Figure 5-29 shows the sensitivity and pseudo-sensitivity of the closed-loop control systems. The frequency regions between the leftmost two and rightmost two of dotted lines in Figure 5-29 show the targeted frequency regions. Both RCSs satisfy the pseudo-sensitivity constraint.

Figure 5-30 shows a close-up of the frequency region where the tracking constraint is active. The figure shows that both the serial and parallel system satisfy the tracking constraint. The figure also shows that the parallel system has a lower pseudo-sensitivity than the serial system for almost the full frequency region of the tracking constraint.

Figure 5-31 shows a close-up of the targeted frequency regions. Both the serial and parallel system has a pseudo-sensitivity lower than the linear system's sensitivity across the full length of both targeted frequency regions. The parallel system has the lowest pseudo-sensitivity in the left targeted frequency region than the serial system, but the pseudo-sensitivity of the two RCSs is similar in the right targeted frequency region.

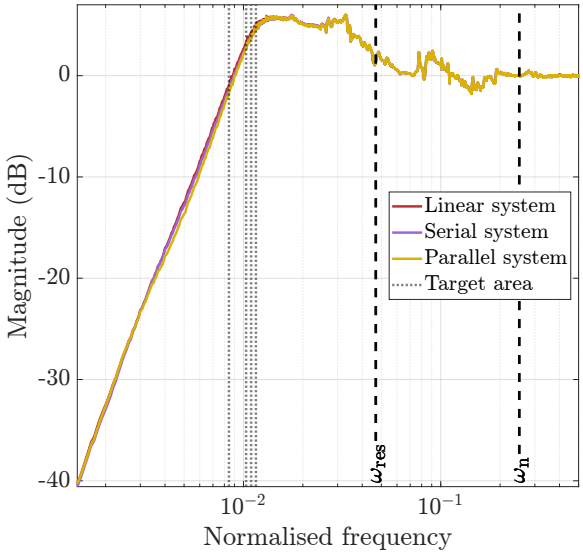

Figure 5-29: Sensitivity and pseudo-sensitivity of the closed-loop control systems.

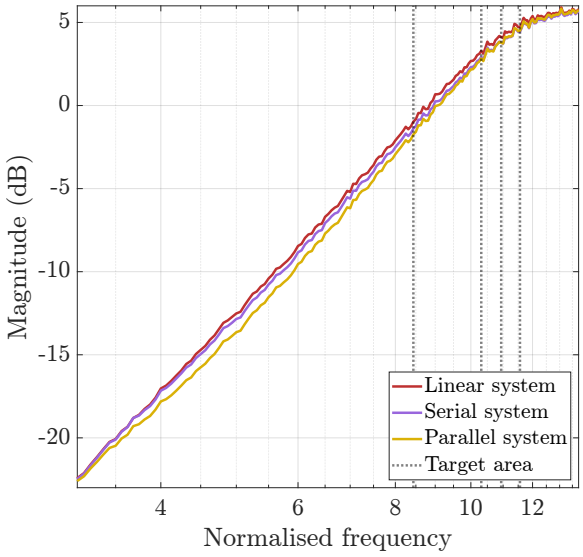

Figure 5-30: Sensitivity and pseudo-sensitivity of the closed-loop control system at the frequency region where the tracking constraint is active.

5-3-5 Time domain analysis

The developed GFbI controllers for the physical wire bonder are tested by having the wire bonder track the reference signal shown in Figure 5-32. The signal consists of one 16 sequential smooth steps, eight up and eight down. After each step, a settling region is defined that starts from the moment the reference signal becomes stationary and runs until all three error signals have converged roughly to within the smallest amplitude they all remain in until the start of the next step or until the end of the reference signal for the last step. The length of each settling region varies after each step. The first settling region is denoted as settling region 1, the second as settling region 2, and so on.

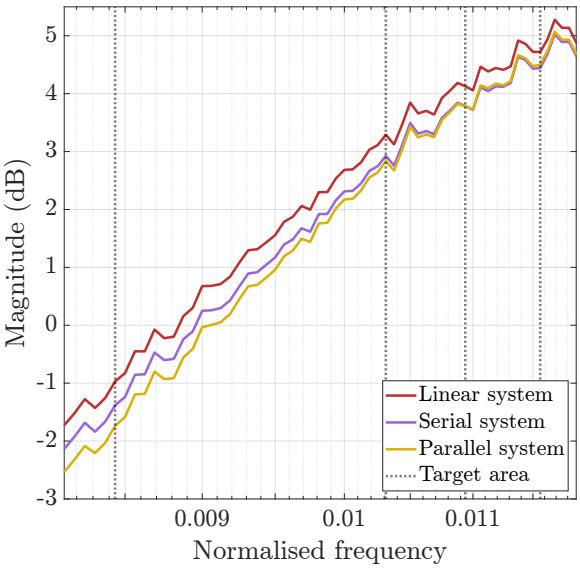

Figure 5-31: Targeted frequency regions of the sensitivity and pseudo-sensitivity of the closed-loop control systems.

Figures 5-33 to 5-36 show the error signal in the settling region for a selection of the steps in the reference signal. All four figures show (part of) the sinusoid sinusoid that underlies the choice for the targeted frequency ranges for the GFA that is used for tuning of the GFbI controllers.

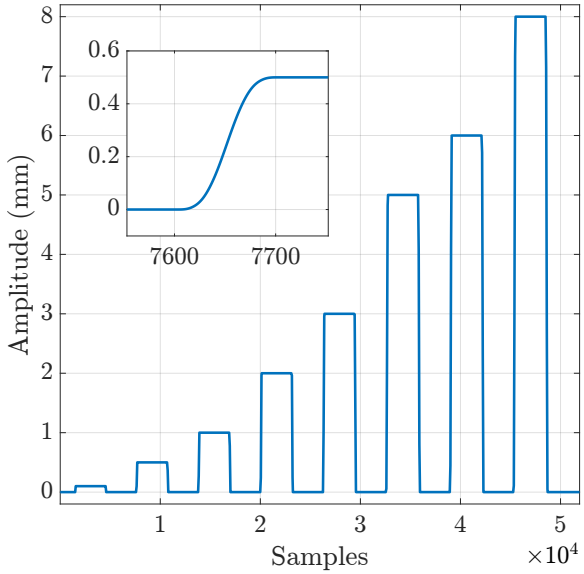

Figure 5-32: Reference signal for validation using the physical wire bonder.

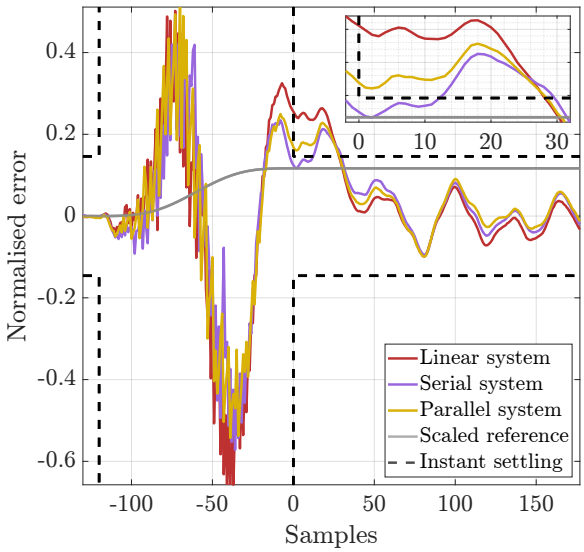

Figure 5-33: Error signal of settling region 7. This is the settling region where the serial system performs the worst in terms of settling time change.

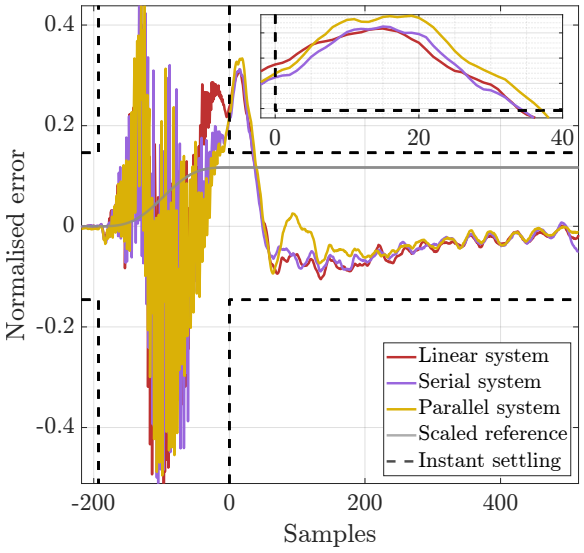

Figure 5-34: Error signal of settling region 11. This is the settling region where the parallel system performs the worst in terms of settling time change.

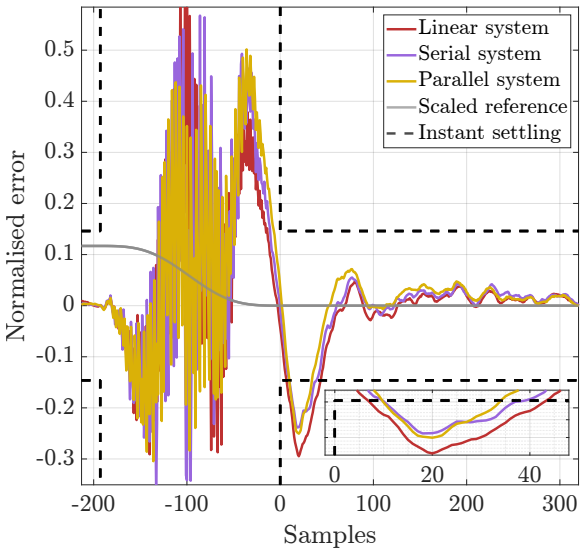

Figure 5-35: Error signal of settling region 12. This is the settling region where the parallel system performs the best in terms of settling time change after settling region 15.

Figure 5-37 shows the CPSD of the error in all settling regions. The power has been normalised such that the maximum power of the linear sys-

tem's CPSD equals 1. Note this is the CPSD from the error signal starting only as soon as the reference signal becomes *stationary*. Of the two systems with a GFbI controller, the parallel system shows to have decreased the power in the error signal the most with respect to the linear system.

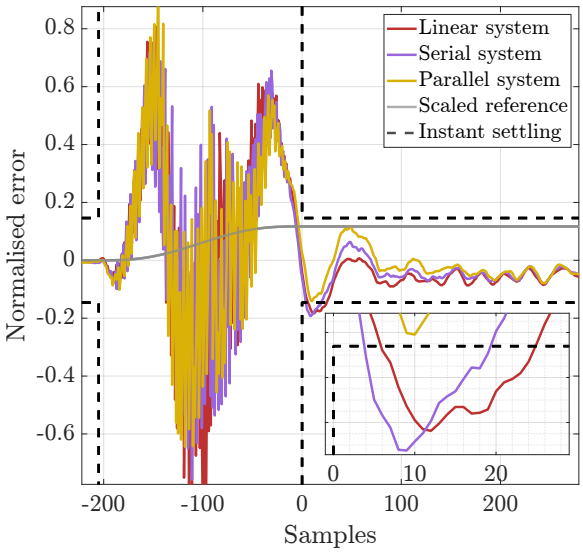

Figure 5-36: Error signal of settling region 15. This is the settling region where the parallel system performs the best in terms of settling time change.

Table 5-7 presents the settling time, measured in samples, for all settling regions. The settling time is defined as the time between the start of the settling region until the error signal crosses the bound for the last time during the settling region. The settling time is interpolated between the last sample outside and inside of the bound. The indicated settling time changes are with respect to the linear system. The settling regions that are visualised in Figures 5-33 to 5-36 are marked in grey.

Table 5-8 presents the RMSE in the settling regions. The RMSE is computed using the normalised error shown in Figures 5-33 to 5-36. The indicated RMSE changes are with respect to the linear system. The settling regions that are visualised in Figures 5-33 to 5-36 are marked in grey.

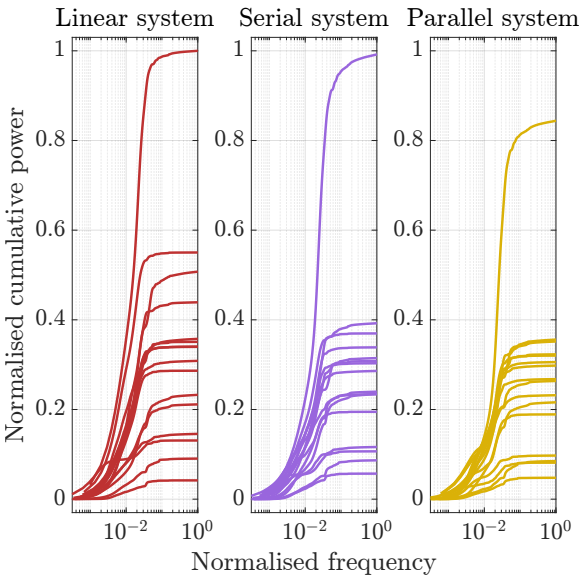

Figure 5-37: Cumulative power spectral density of the error in both settling regions padded with zeros ten times the length of the error signal and convolved with a rectangular window.

Table 5-9 presents statistics based on the settling time and RMSE of all settling regions. In one settling region, the parallel system is able to achieve instant settling whereas the other two control systems do not. Both the serial and parallel system outperform the linear system in terms of median settling time and RMSE, where the parallel system performs better than the serial system. The same is true for the median RMSE.

Table 5-9: Statistics based on the settling time and RMSE of Tables 5-7 and 5-8.

Metric	Serial system	Parallel system
Best settling time change (%)	-22.243	-100.000
Worst settling time change (%)	+5.178	+8.790
Median settling time change (%)	-5.475	-9.791
Median RMSE change (%)	-5.374	-9.455

Table 5-7: Settling time after each step in the reference signal.

Settling region	Settling time linear system (samples)	Settling time serial system (samples)	Settling time parallel system (samples)	Change serial system (%)	Change parallel system (%)
1	42.300	42.000	42.529	-0.710	+0.542
2	45.345	44.609	43.524	-1.623	-4.016
3	45.588	45.944	44.722	+0.781	-1.900
4	49.692	49.038	48.579	-1.316	-2.241
5	44.267	44.424	42.795	+0.356	-3.325
6	51.860	53.234	50.067	+2.649	-3.459
7	28.143	29.600	28.387	+5.178	+0.368
8	52.695	52.852	49.855	+0.298	-5.390
9	20.875	20.647	17.333	-1.092	-16.968
10	48.968	44.955	40.182	-8.196	-17.942
11	34.120	34.500	37.119	+1.114	+8.790
12	43.391	39.000	34.057	-10.120	-21.512
13	30.241	29.041	30.020	-3.969	-0.732
14	26.878	25.194	25.378	-6.264	-5.580
15	24.864	19.333	0.000	-22.243	-100.000
16	0.000	0.000	0.000	0.000	0.000

Table 5-8: RMSE for all settling regions.

Settling region	RMSE linear system (normalised)	RMSE serial system (normalised)	RMSE parallel system (normalised)	Change serial system (%)	Change parallel system (%)
1	0.0695	0.0743	0.0779	+6.831	+12.124
2	0.0727	0.0731	0.0703	+0.542	-3.360
3	0.0881	0.0881	0.0837	-0.0152	-4.948
4	0.0880	0.0833	0.0784	-5.313	-10.950
5	0.0892	0.0838	0.0857	-6.144	-3.955
6	0.0999	0.0945	0.0894	-5.435	-10.499
7	0.107	0.0847	0.0901	-21.058	-16.020
8	0.151	0.150	0.138	-0.613	-8.411
9	0.0574	0.0513	0.0469	-10.678	-18.285
10	0.112	0.0918	0.0852	-18.036	-23.904
11	0.0836	0.0805	0.0820	-3.738	-1.854
12	0.0806	0.0664	0.0653	-17.632	-18.898
13	0.0899	0.0728	0.0724	-19.050	-19.523
14	0.0452	0.0442	0.0438	-2.216	-3.074
15	0.0551	0.0496	0.0432	-9.977	-21.643
16	0.0308	0.0359	0.0328	+16.540	+6.670

5-3-6 Overall analysis

The GFbI controllers for the physical wire bonder were optimised on the same machine as the simulated wire bonder. The runtime of the GFA to optimise GFbI controllers for the physical wire bonder was roughly 20 hours per controller. Optimising the controllers for the physical wire bonder takes longer than for the simulated wire bonder, as the FRF of the former is significantly longer than that of the latter, resulting in a higher computational cost for each candidate GFbI controller and requiring more function evaluations for convergence of the solution. The solution for the serial GFbI controller was found by `particle swarm` combined with `simulated annealing`. The solution for the parallel GFbI controller was found by `surrogate optimisation`. Note that "fevals" includes function calls by `pattern search`, which clarifies the difference between the serial and parallel GFbI controller optimisation. Table 5-10 presents further information on the found solution and optimisation procedure. Numerical values for other controller element parameters are redacted.

The results of the validation with the physical wire bonder is similar to the validation with the simulated wire bonder. All constraints are satisfied, assumptions 1, 2 and 3 hold in the same manner, and the pseudo-sensitivity is close to the sensitivity of the SIDF in the RCSs. Additionally, the same conclusions can be drawn regarding the sequence of the GFbI controller.

Table 5-10: Data of the optimisation procedure and found solution of the GFbI controllers.

	Serial	Parallel
Final cost (dB)	-0.278	-0.220
fevals	47268	10689
γ	0.774	0.365
ω_c/ω_i	0.567	0.596

For the validation with the physical wire bonder, the optimisation target of the GFA is leveraged to reduce the settling time. Similarly to the validation with the simulated wire bonder, frequency-domain performance prediction suggests the GFbI controllers both should do so better than the linear system, again with the parallel GFbI controller showing the most promising prediction. The time-domain results confirm the performance prediction, where indeed the settling time has decreased for both the serial and parallel system. Additionally, the RMSE decreased, too. The parallel system outperforms the serial system again in both the median settling time and median RMSE.

Chapter 6

Conclusion and future research recommendations

This chapter provides a conclusion on this work and the validation thereof in Section 6-1. Additionally, future research recommendations are provided in Section 6-2.

6-1 Conclusion

The tuning of reset controllers is a cumbersome and time-consuming task. There are no established tuning rules, and even if there were, such rules generally lead to sub-optimal designs. This work provides two contributions aimed at maximising the use of the beneficial reduced phase lag of reset control to improve upon the performance of linear control in an automated fashion. Although various reset controller structures exist that can be designed based solely on the plant FRF, the GFbI element is the only reset element for which the effects of higher-order harmonics can be taken into account in the controller design, and that does not require trading off the the advantageous reduced phase lag near the bandwidth frequency and reducing the generation of higher-order harmonics. Therefore, this work focuses on the tuning of reset controllers containing a GFbI element.

The first contribution is a comparative study on the effect of the sequence of the controller elements in a reset controller containing a lead filter. The reset element generates higher-order harmonics that propagate through the rest of the controller. A lead filter amplifies the negative impact on the error signal of these higher-order harmonics. Commonly, reset controllers are designed such that all controller elements are placed in series with the reset element as the first controller element to prevent the amplification of measurement noise. The output of the reset element then passes through the lead filter in both open loop and closed loop. By placing the reset element and lead filter in parallel instead, the higher-order harmonics do not pass through the lead filter and their negative impact on the error signal is decreased. In this work, it was investigated what the effects of using the aforementioned serial and parallel sequence are on the tuning of a reset controller containing a GFbI element.

The second contribution is the proposal of a tuning algorithm to optimise the performance of a controller containing a GFbI element programmatically. The algorithm uses an equally-well-tuned reference linear controller as a baseline for the performance based on frequency-domain performance prediction and ensures the tuned reset controller performs at least as well as the refer-

ence linear controller based on frequency-domain performance prediction metrics. Additionally, one or multiple frequency regions can be specified for which the algorithm attempts to minimise the pseudo-sensitivity of the reset controller using the sensitivity of the reference linear controller as a weight. This can be used to suppress specific vibrations observed beforehand in the error signal.

The contributions are validated using two use cases, namely tracking a reference signal with a simulated wire bonder and with a different, physical wire bonder. The tuning algorithm proved able to successfully tune two reset controllers for each plant, namely one in which the controller elements are placed in series and another in which the reset element and lead filter are placed in parallel. The reset control systems satisfy the same constraints as the reference linear system. Additionally, the pseudo-sensitivity of the reset control systems is successfully reduced to below the sensitivity of the reference linear system for all frequencies in all targeted frequency regions, indicating increased suppression of the observed vibrations in the error signal. The results of time-domain simulations and experiments on a physical setup confirmed the performance prediction when comparing the tuned reset controllers to the reference linear system. The use case with the goal of suppressing a dominant vibration in the error signal showed a reduced median RMSE of 16.245 % while the median settling time did not increase, but rather decreased as well by 3.671 %. The use case with the goal of reducing the settling time showed a median reduction in the settling time of 9.791 %, while the median RMSE also decreased by 9.455 %. Across both use cases and both in performance prediction and time-domain results, the reset control system with the parallel sequence reset controller outperformed that with the serial sequence reset controller.

The validation results highlight the potential of reset control as a means to overcome inherent limitations of linear systems. Using two industrially realistic use cases, automatically tuned reset controllers with a GFbI element were able to improve upon the performance of automatically tuned linear controllers. A key feature therein is proper tuning of the reset controllers. The proposed tuning algorithm was shown to successfully tune four different reset controllers containing a GFbI element that had either a serial or parallel sequence of the controller elements. In tracking a reference signal that first moves smoothly and then becomes stationary, all tuned reset controllers showed a reduced RMSE and settling time compared to the reference linear controller, confirming the predicted performance increase. Between a serial or parallel sequence, the parallel sequence showed the best performance, indicating that preventing the generated higher-order harmonics from passing through a lead filter indeed reduces the negative effects thereof.

6-2 Future research recommendations

There are several recommendations for future research based on this work and the validation thereof.

1 | Stability check
The GFA does not have a method to check for the stability of an RCS with a candidate GFbI controller. Therefore, it also does not penalise unstable controllers and the control system designer needs to select bounds for the optimisation parameters such that no unstable GFbI controller can be designed with any combination of the optimisation parameters. This severely limits the possible design space of the global optimisation algorithms and might consequently lead to missing better controller parameters, as they would be outside of the bounds. By adding a stability check and adding the stability of the RCS as a constraint, the design space may be expanded and perhaps better GFbI controllers may be found.

During the development of the GFA, it happened on occasion that the GFA was run and found an RCS that could not be simulated or the pseudo-sensitivy showed undesired behaviour, indicating the RCS was unstable. It was never investigated whether the BLS of such an RCS was stable or unstable. It is possible that the instability of the RCS was caused by an unstable BLS. A possible solution might be to add a stability check for the BLS of a candidate RCS, as perhaps stability thereof

might be sufficient to remove the related restriction on the bounds of the optimisation parameters.

2 | Effect of controller sequence
The effect of using a serial or parallel sequences has only been validated by comparing the corresponding GFbI controllers tuned by the GFA. Those GFbI controllers have significantly more differences than only the sequence of the controller elements, as the optimisation parameters were tuned for each GFbI controller. As such, it cannot definitively be concluded what the effect of only changing the sequence is. The results have shown the parallel GFbI controller to outperform the serial GFbI controller in both the time domain and frequency domain. However, the results have also shown that the sensitivity of the HOSIDFs of the parallel GFbI controller are higher than that of the serial GFbI controller in the low-frequency region. Thus, it might be possible that for different targeted frequency regions or for a different plant a serial sequence allows for better performance of the subsequently tuned GFbI controller.

3 | Optimal controller sequence
A serial sequence and parallel sequence are the only sequences investigated in this work. The point of the parallel sequence is to avoid passing the generated higher-order harmonics through the lead filter in open loop. However, placing the lead filter in parallel with the reset element is not the only method to do so. For example, the lead filter may also be placed before the reset element. A drawback of this is that measurement noise is amplified, which could degrade performance. Whether such a sequence would result in improved performance will need to be researched.

4 | Free variables of parallel sequence
The parameters of a parallel controller are determined by their relation to the parameters of the serial controller given in (3-5). The implementation of the GFA used in this work changes the parameters of a parallel GFbI controller indirectly, namely by changing the parameters of a serial controller and computing the corresponding parameters for a parallel controller through (3-5). However, as shown in Figure 3-3, a parallel controller has more parameters in total. With the described implementation of constructing a parallel GFbI controller, those extra parameters are unused and fully determined by the other parameters. By *directly* changing *all* the parameters of a parallel controller, the GFA obtains more degrees of freedom to tune to obtain an optimal parallel GFbI controller. This might result in the GFA finding better solutions than it is able to with the current implementation. A drawback of the proposed method, however, is that the increased number of parameters will inevitably lead to a longer runtime of the GFA for optimising a parallel GFbI controller.

5 | Improving the transient response
In optimisation of the GFbI controllers for the simulated wire bonder, the targeted frequency region was chosen such that the base frame vibration, that was clearly visible in the error signal, would be suppressed. For the physical wire bonder, no such clear vibration could be observed in the settling region of the error signal. Therefore, a targeted frequency region was chosen that contains the frequency of the sinusoid observed near the end of the tracking region, although this sinusoid is primarily part of the transient response. The aim of this targeted frequency region was to reduce the settling time. As it turned out, significantly reducing the settling time is difficult, as only half or even only a quarter of the sinusoid could be observed *in the settling region*, after which the error signal has already settled to within specifications. To further improve the settling time, research is needed into improvement of the transient response, as the point at which the error signal settles is considerably close to the tracking region.

6 | Optimisation parameter scaling
In the used implementation of the GFA, the optimisation parameters are changed as-is by the various global and local optimisation algorithms. Some optimisation algorithms are known to show increased performance when their optimisation parameters p_i with i parameters are all scaled to equal-sized domains, e.g. $p_i \in [-1, 1]$. The optimisation parameters used in these case studies for the GFA range from the order of 10^0 to 10^8. The difference in these orders of magnitude suggests scaling the optimisation parameters might improve the performance of the GFA.

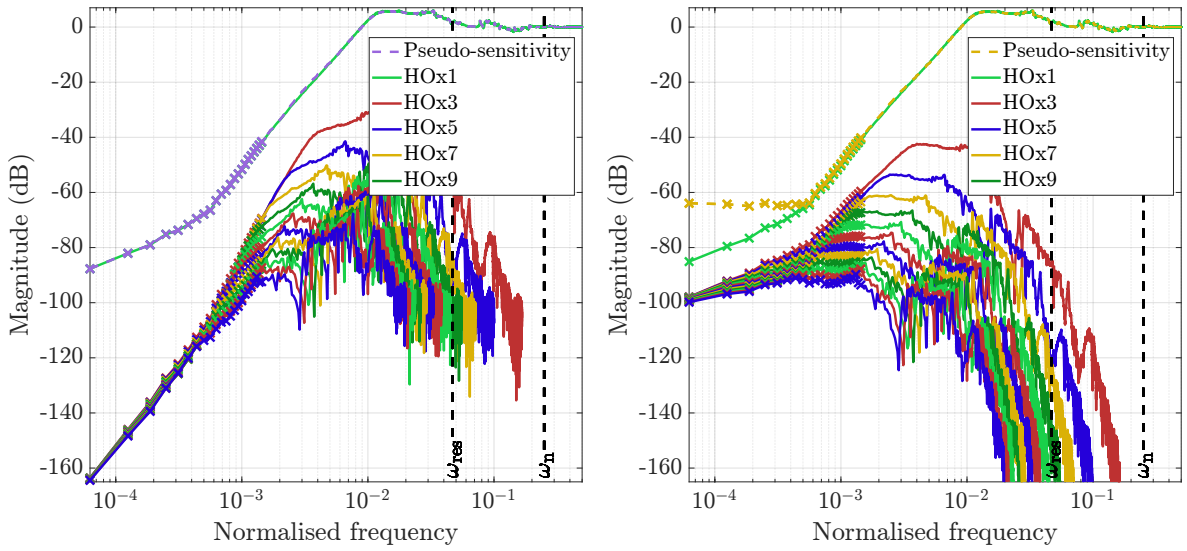

(a) RCS with a serial GFbI controller.

(b) RCS with a parallel GFbI controller.

Figure 6-1: Pseudo-sensitivity and HOSIDF sensitivities of GFbI controllers with a slightly higher ω_{skip} than used for validation. The crosses denote frequencies for which assumption 2 does not hold. The frequency ω_{skip} lies just after the rightmost cross.

7 | Diverging pseudo-sensitivity

Specific to the use case of the physical wire bonder, a parallel GFbI controller tuned with a slightly higher ω_{skip} than the value used for validation produces a remarkable result. Presumably due to the increased-magnitude sensitivity of the HOSIDFs compared to the RCS with a serial GFbI controller, the pseudo-sensitivity below a certain frequency lower than ω_{skip} strays away from the sensitivity of the SIDF, whereas for any higher frequencies, the pseudo-sensitivity remains in the vicinity of the sensitivity of the SIDF. This is illustrated in Figures 6-1 and 6-2. As shown, assumption 2 does not hold for frequencies below ω_{skip}. Even though the pseudo-sensitivity is invalid at those frequencies and the cost in the GFA of this GFbI controller is slightly lower than for a slightly lower ω_{skip}, for the invalid-pseudo-sensitivity to stray away from the sensitivity of the SIDF is undesired. Whether this is problematic for the performance of the controller needs to be further investigated. If research shows it does have a bad influence on any of those two traits, it might be resolved by constraining the pseudo-sensitivity to not be higher than a certain value above the sensitivity of the SIDF for all $\omega < \omega_{skip}$ or not be higher at all.

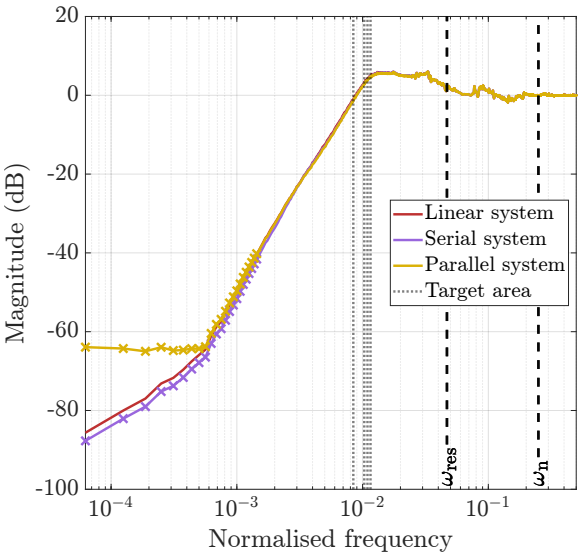

Figure 6-2: Sensitivity of the control system with the reference linear controller and pseudo-sensitivities of the RCS with a serial or parallel GFbI controllers that is tuned with a slightly higher ω_{skip} than used for validation. The crosses denote frequencies for which assumption 2 does not hold. The frequency ω_{skip} lies just after the rightmost cross.

Bibliography

[1] K. Åström and T. Hägglund, "The future of PID control," *Control Engineering Practice*, vol. 9, no. 11, pp. 1163–1175, 2001, PID Control. DOI: 10.1016/S0967-0661(01)00062-4.

[2] M. M. Seron, J. H. Braslavsky, and G. C. Goodwin, *Fundamental Limitations in Filtering and Control*. London: Springer, 1997, ISBN: 3540761268.

[3] J. Freudenberg, R. Middleton, and A. Stefanpoulou, "A survey of inherent design limitations," in *Proceedings of the 2000 American Control Conference. ACC*, vol. 5, 2000, 2987–3001 vol.5. DOI: 10.1109/ACC.2000.879113.

[4] O. Beker, "Analysis of Reset Control Systems," Ph.D. dissertation, University of Massachusetts, 2001.

[5] J. C. Clegg, "A nonlinear integrator for servomechanisms," *Transactions of the American Institute of Electrical Engineers, Part II: Applications and Industry*, vol. 77, no. 1, pp. 41–42, 1958. DOI: 10.1109/TAI.1958.6367399.

[6] Y. Guo, Y. Wang, and L. Xie, "Frequency-Domain Properties of Reset Systems With Application in Hard-Disk-Drive Systems," *IEEE Transactions on Control Systems Technology*, vol. 17, no. 6, pp. 1446–1453, 2009. DOI: 10.1109/TCST.2008.2009066.

[7] N. Saikumar, K. Heinen, and S. H. HosseinNia, "Loop-shaping for reset control systems: A higher-order sinusoidal-input describing functions approach," *Control Engineering Practice*, vol. 111, p. 104 808, 2021. DOI: 10.1016/j.conengprac.2021.104808.

[8] A. A. Dastjerdi, A. Astolfi, N. Saikumar, N. Karbasizadeh, D. Valério, and S. H. HosseinNia, "Closed-Loop Frequency Analysis of Reset Control Systems," *IEEE Transactions on Automatic Control*, vol. 68, no. 2, pp. 1146–1153, 2023. DOI: 10.1109/TAC.2022.3184039.

[9] H. Hosseinnia, I. Tejado, D. Torres, B. Vinagre, and V. Feliu, "A general form for reset control including fractional order dynamics," *IFAC Proceedings Volumes (IFAC-PapersOnline)*, vol. 19, pp. 2028–2033, Jan. 2014.

[10] A. Baños and A. Vidal, "Definition and tuning of a PI+CI reset controller," in *2007 European Control Conference (ECC)*, 2007, pp. 4792–4798. DOI: 10.23919/ECC.2007.7068602.

[11] L. F. van Eijk, Y. Liu, X. Zhang, D. Kostić, and S. H. HosseinNia, "A Nonlinear Integrator Based on the First-Order Reset Element," *IFAC-PapersOnLine*, 2024 (in press), 4th IFAC Conference on Advances in Proportional-Integral-Derivative Control.

[12] L. F. van Eijk, S. Beer, R. M. J. van Es, D. Kostić, and H. Nijmeijer, "Frequency-Domain Properties of the Hybrid Integrator-Gain System and Its Application as a Nonlinear Lag Filter," *IEEE Transactions on Control Systems Technology*, vol. 31, no. 2, pp. 905–912, 2023. DOI: 10.1109/TCST.2022.3196878.

[13] S. A. Hosseini, M. S. Tavazoei, L. F. Van Eijk, and S. H. HosseinNia, "Generalizing Hybrid Integrator-Gain Systems Using Fractional Calculus," in *2022 IEEE Conference on Control Technology and Applications (CCTA)*, 2022, pp. 1050–1055. DOI: 10.1109/CCTA49430.2022.9966184.

[14] K. J. Åström and R. M. Murray, *Feedback systems: An Introduction for Scientists and Engineers*. Princeton University Press, 2012. DOI: 10.5860/choice.46-2107.

[15] R. M. Schmidt, G. Schitter, A. Rankers, and J. van Eijk, *The Design of High Performance Mechatronics*, 3rd ed. Delft University Press, 2020, ISBN: 978-1-64368-050-7.

[16] S. Skogestad and I. Postlethwaite, *Multivariable Feedback Control - Analysis and Design*, Second. John Wiley & Sons, 2001. DOI: 10.1109/MCS.2007.284514.

[17] G. Stein, "Respect the unstable," *IEEE Control Systems Magazine*, vol. 23, no. 4, pp. 12–25, 2003. DOI: 10.1109/MCS.2003.1213600.

[18] E. Akyüz, N. Saikumar, and S. H. HosseinNia, "Reset Control for Vibration Disturbance Rejection," *IFAC-PapersOnLine*, vol. 52, no. 15, pp. 525–530, 2019, 8th IFAC Symposium on Mechatronic Systems MECHATRONICS 2019. DOI: 10.1016/j.ifacol.2019.11.729.

[19] N. Saikumar, R. K. Sinha, and S. H. HosseinNia, ""Constant in Gain Lead in Phase" Element–Application in Precision Motion Control," *IEEE/ASME Transactions on Mechatronics*, vol. 24, no. 3, pp. 1176–1185, 2019. DOI: 10.1109/TMECH.2019.2909082.

[20] A. A. Dastjerdi, A. Astolfi, and S. H. HosseinNia, "Frequency-domain stability methods for reset control systems," *Automatica*, vol. 148, p. 110 737, 2023. DOI: 10.1016/j.automatica.2022.110737.

[21] T. Kubota, N. Hori, T. Nguyen-Van, and S. Kawai, "Discretization Accuracy of Mapping Models in Closed-Loop," in *2021 IEEE 10th Global Conference on Consumer Electronics (GCCE)*, 2021, pp. 885–889. DOI: 10.1109/GCCE53005.2021.9622002.

[22] "When to Use a Hybrid Function," MathWorks. (2024), [Online]. Available: https://www.mathworks.com/help/gads/when-to-use-hybrid-function.html (visited on 05/06/2024).

[23] "Particle Swarm," MathWorks. (2024), [Online]. Available: https://www.mathworks.com/help/gads/particle-swarm.html (visited on 05/06/2024).

[24] "Genetic Algorithm," MathWorks. (2024), [Online]. Available: https://www.mathworks.com/help/gads/genetic-algorithm.html (visited on 05/06/2024).

[25] "Surrogate Optimisation," MathWorks. (2024), [Online]. Available: https://www.mathworks.com/help/gads/surrogate-optimization.html (visited on 05/06/2024).

[26] "Simulated Annealing," MathWorks. (2024), [Online]. Available: https://www.mathworks.com/help/gads/simulated-annealing.html (visited on 05/06/2024).

[27] "Direct Search," MathWorks. (2024), [Online]. Available: https://www.mathworks.com/help/gads/direct-search.html (visited on 05/06/2024).

[28] M. Schuettler and T. Stieglitz, "4 - Microassembly and micropackaging of implantable systems," in *Implantable Sensor Systems for Medical Applications*, ser. Woodhead Publishing Series in Biomaterials, A. Inmann and D. Hodgins, Eds., Woodhead Publishing, 2013, pp. 108–149, ISBN: 978-1-84569-987-1. DOI: 10.1533/9780857096289.1.108.

[29] Y. Liu, "Automated reset controller design with a novel structure for improved performance of an industrial motion stage," M.S. thesis, Delft University of Technology, 2023.

Glossary

List of Acronyms

LTI	linear time-invariant
NLTI	nonlinear time-invariant
SISO	single-input single-output
FRF	frequency response function
SIDF	sinusoidal-input describing function
HOSIDF	higher-order SIDF
BLS	base linear system
GFA	GFbI feedback autotuner
UBIBS	uniformly bounded-input bounded-state
NSV	Nyquist stability vector
RMSE	root-mean-square error
DoF	degrees of freedom
PSD	power spectral density
CPSD	cumulative PSD
PI	proportional-integral
PID	proportional-integral-derivative
CI	Clegg integrator
PCI	proportional Clegg integrator
GFORE	generalised first-order reset element
GSORE	generalised second-order reset element
SOSRE	second-order single-state reset elements
GFbI	GFORE-based integrator
PGFbI	proportional GFORE-based integrator
HIGS	hybrid integrator-gain systems
RCS	reset control system